IEEE Transactions on Robotics (T-RO) paper, presented at ICRA 2026, Vienna, Austria. Cite as T-RO paper.

A Single Hydraulic Bellows-based MRI-safe Robotic Needle Driver Capable of Independent and Coupled Needle Translation and Rotation

Yufu Qiu[1], Haiyang Fang[1], Kwan Kit Lin[1], and Shing Shin Cheng[1,2*]

***Abstract*—Despite decades of research in magnetic resonance imaging (MRI)-compatible robotic technologies, the existing MRI-safe needle drivers rarely feature simultaneously high compactness, large insertion force, and motion versatility, all of which are critical to facilitate clinical translation in intraoperative MRI-guided percutaneous procedures. The paper presents an MR-safe needle driver that for the first time offers all these desired qualities. It measures only 2.2 × 5.3 × 3.8 cm (length × width × height), facilitating its adoption in in-bore skull-mounted or body-mounted MRI-guided procedures. It is driven by a single hydraulic bellows-based actuator, which provides good water sealing, smooth motion, and high expansion ratio, and a pre-clamped gripper design that offers large insertion force (>10 N). A compact passive rotation mechanism, together with a motion decoupling and switching mechanism, was introduced, allowing the needle to move with three motion types: independent translation, translation with passive rotation, and independent rotation. The passive rotation motion reduces needle deformation and tissue resistance during insertion, while the combination of independent translation and independent rotation enables flexible needle steering. An adaptive elastic fuzzy controller was further developed to address the limitation of encoder resolution and the unknown nonlinear dynamics of the hydraulic bellows-based actuator to provide accurate needle tip control (<0.06 mm overshoot and 0.17 mm root-mean-square repeatability error). The compact and highly versatile needle driver design with its high motion accuracy represents a significant breakthrough in MRI-safe robotic technology, facilitating in-bore real-time MRI-guided interventions that could save MRI operation time, improve workflow efficiency, and enable more autonomy integration.**

I. Introduction

Percutaneous interventional procedures are crucial in modern surgery and widely used in treatments such as puncture biopsy, tumor ablation, and electrode placement. These procedures typically require high precision and are performed by a skilled physician under the guidance of medical images [1]. Among the common medical imaging modalities, magnetic resonance imaging (MRI) uniquely provides high resolution images and high soft tissue contrast, allows thermal monitoring, and does not expose patients and clinicians to ionising radiation [2].

MRI-compatible percutaneous robotic systems have been investigated in the past decades to improve needle targeting accuracy by leveraging robotic precision and MR image/thermal guidance. Most of these robots are purely needle positioning or guiding systems, which can adjust the needle trajectory before the physician manually inserts the needle. For example, Meinhold et al. proposed a needle positioning platform based on a two-layer parallel frame actuated by linear piezoelectric motors [3]. Li et al. proposed a piezoelectric motor-actuated neurosurgical needle positioning platform with a 3-degree of freedom (DOF) Cartesian platform and a 2 DOFs remote center of motion (RCM) mechanism [4]. Franco et al. presented a 4 DOFs needle guiding platform based on pneumatic plastic cylinders for liver ablation [5], while Stoianovici et al. developed a needle-guide robot with 2 DOFs RCM constraint [6] actuated by pneumatic stepper motors. Guo et al. proposed a needle positioning robot using rolling diaphragms-based hydraulic actuators for bilateral stereotactic neurosurgery [7]. He et al. introduced a hydraulics-actuated RCM-constrained soft needle guide robot with a locking mechanism [8]. However, when using these robotic platforms, the patients need to be moved out of the MRI bore to allow the clinicians to manually insert the needle and back into the MRI bore for needle placement verification after each insertion. This significantly increases the workflow complexity and procedure time, thus limiting the potential for clinical translation. The lack of a robotic needle driver prevents the needle insertion process to be performed in-bore under the MR image guidance, and further limits the integration of any automated or semi-autonomous control framework for percutaneous procedure.

In the recent decade, several MRI-compatible robotic needle drivers have been developed and integrated with the positioning platforms, mostly for prostate or breast procedures [9]–[12]. A popular needle driver design is to attach the needle to a piston-cylinder system, which drives the needle when positive fluid pressure is applied [13]–[16]. However, the use of the fluid cylinder typically results in a relatively long needle driver, limiting its application to procedures in which the needle driver is placed along the longitudinal axis of the MRI bore. During body-mounted procedures (e.g. spinal injection) and head-mounted procedures (e.g. intracranial biopsy), the needle is

Research reported in this work was supported in part by Innovation and Technology Commission of Hong Kong (ITS/235/22, ITS/225/23, ITS/224/23, MHP/096/22 and Multi-scale Medical Robotics Center (InnoHK Initiative)), and in part by Research Grants Council of Hong Kong (CUHK 14217822, CUHK 14207823, CUHK 14211425, T45-401/22-N and AoE/E-407/24-N). The content is solely the responsibility of the authors and does not necessarily represent the official views of the sponsors. *Corresponding author: Shing Shin Cheng. (email: sscheng@cuhk.edu.hk)

[1]Yufu Qiu, Haiyang Fang, Kwan Kit Lin, and Shing Shin Cheng are with Department of Mechanical and Automation Engineering and T Stone Robotics Institute, The Chinese University of Hong Kong, Hong Kong.

[2]Shing Shin Cheng is with Shun Hing Institute of Advanced Engineering and Multi-Scale Medical Robotics Center, The Chinese University of Hong Kong, Hong Kong.

IEEE Transactions on Robotics (T-RO) paper, presented at ICRA 2026, Vienna, Austria. Cite as T-RO paper.

typically inserted radially within the MRI bore or head coil, which imposes a strict requirement on the size, especially height, of the needle driver. Researchers have proposed more compact needle drivers that operate in constrained working space. Hungr et al. utilized a Bowden cable connected to an ultrasonic motor to adjust the displacement of a depth stopper and pneumatic piston-cylinders to drive the needle [17], while Wu et al. and wang et al. utilized a beaded chain connected to a remotely placed ultrasonic motor [18], [19] to drive a spinal injection needle. However, the use of these transmission mechanisms makes the needle driver systems bulky and heavy, increasing the stiffness demand on the needle positioning platform that holds the needle driver [20]. These mechanisms also introduce additional mechanical components, which lead to high friction, particularly when the needle driver is not parallel to the transmission mechanism.

Other researchers have developed needle drivers based on the inchworm-based working principle, which enable their size to be significantly reduced. These needle drivers make use of a toroidal bellows-based flexible fluidic actuator (FFA) [21], an auxetic structure-based linear actuator [22], and a double-acting hydraulic bellows linear actuator [23]. However, these inchworm motion-based needle drivers provide relatively small insertion force due to the slippage between the gripper and the needle. While significant progress has been made in the development of MRI-compatible needle drivers, most still do not offer a combination of high compactness, minimal setup complexity, and high insertion force.

Additionally, many existing MRI-compatible needle drivers only provide translation motion for the needle. Needle rotation however should be an important DOF incorporated into an MR-compatible needle driver to provide more versatile functions as follows. First, simultaneous needle translation and rotation could reduce tissue resistance by approximately 15% [24], leading to improved tissue penetration effectiveness. Second, simultaneous needle rotation and translation can reduce needle deflection and ensure improved linearity of the needle trajectory, as shown by the works by Abolhassani et al. [25] and Minhas et al. [26]. Third, needle rotation can also be used to enable needle steering of a flexible bevel-tipped needle [27], [28] by adjusting the bevel tip direction, thus producing a curvilinear trajectory that circumvents critical regions during the needle insertion into a deep anatomical target. Comber et al. have developed an MR-safe needle driver with 2 DOFs (i.e., translational and rotational) motion [29], but their design features slow operational speed and also requires an additional actuator for the rotation mechanism, resulting in a bulky and elongated overall setup unsuitable for body-mounted or skull-mounted MRI-guided robotic procedures. Besides, its 2 DOFs are independent of each other, preventing simultaneous translational and rotational motions that would enable functions 1 and 2 mentioned above.

Overall, existing MR-compatible needle drivers could not achieve high compactness, high force, and high accuracy simultaneously and most offer only translation motion. In light of these limitations, this article presents an MR-safe robotic needle driver, incorporating various combinations (independent and coupled) of translation and rotation motions

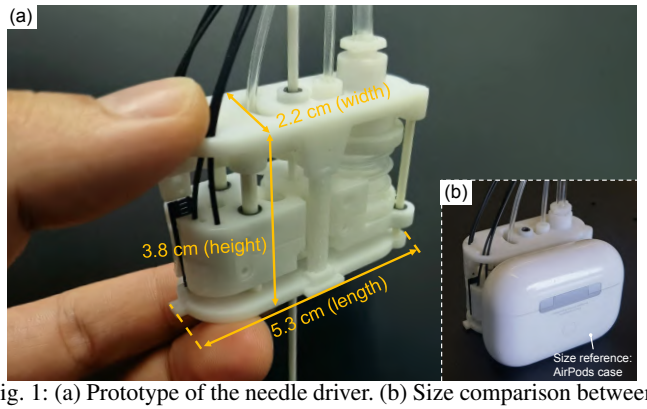

Fig. 1: (a) Prototype of the needle driver. (b) Size comparison between the needle driver and an Apple AirPods Pro charging case.

using a single hydraulic bellows-based linear actuator operating under an adaptive fuzzy controller. The needle driver is highly compact with only 3.8 cm in height, facilitating its integration into body-mounted or skull-mounted needle positioning platforms. To the best of the authors' knowledge, this is not only the most compact needle driver among existing MR-safe (highest MR safety rating without restriction) or MR-conditional (MR safety rating with specific imaging or other conditional requirements) [30] needle drivers, it is also the most versatile due to its ability to produce three motion types, including pure needle translation, simultaneous needle translation and rotation, and pure needle rotation, thus achieving functions, including minimizing needle deflection, enabling effective tissue penetration, and forming curvilinear needle trajectories. The three novel contributions of this paper include:

1) Designing an MR-safe needle driver that incorporates a single hydraulic bellows-based linear actuator, the inch-worm motion concept, and a pre-clamped silicone diaphragm-based needle gripper to simultaneously achieve high compactness (only 3.8 cm height) critical for many skull/body-mounted procedures and high insertion force ($\sim$10 N) sufficient for most percutaneous procedures. Compared with other similarly compact needle driver [22], our needle driver is capable of 5 times the needle insertion force.

2) Introducing a translation with passive rotation mechanism and a motion decoupling mechanism, which enable the needle driver to achieve three motion types, including independent translation, simultaneous translation and passive needle rotation, and independent needle rotation, under a single linear actuator control. Compared with the state-of-the-art MR-safe needle drivers with translation and rotation DOFs [29], our needle driver is significantly more compact (nearly 9 times shorter along the needle axis) and enables both sequential and simultaneous translation and rotation, with the former allowing flexible needle steering and the latter facilitating straight insertion and improved tissue penetration.

3) Designing a filtered observer-based adaptive elastic fuzzy (FO-AEF) controller that overcomes nonlinear behavior of the hydraulic bellows-actuated needle driver (e.g. uncertain dead-zone characteristics, unknown nonlinear system dynamics and hysteresis) and the limitation from 0.5 mm encoder resolution to perform accurate position control of the needle driver.

IEEE Transactions on Robotics (T-RO) paper, presented at ICRA 2026, Vienna, Austria. Cite as T-RO paper.

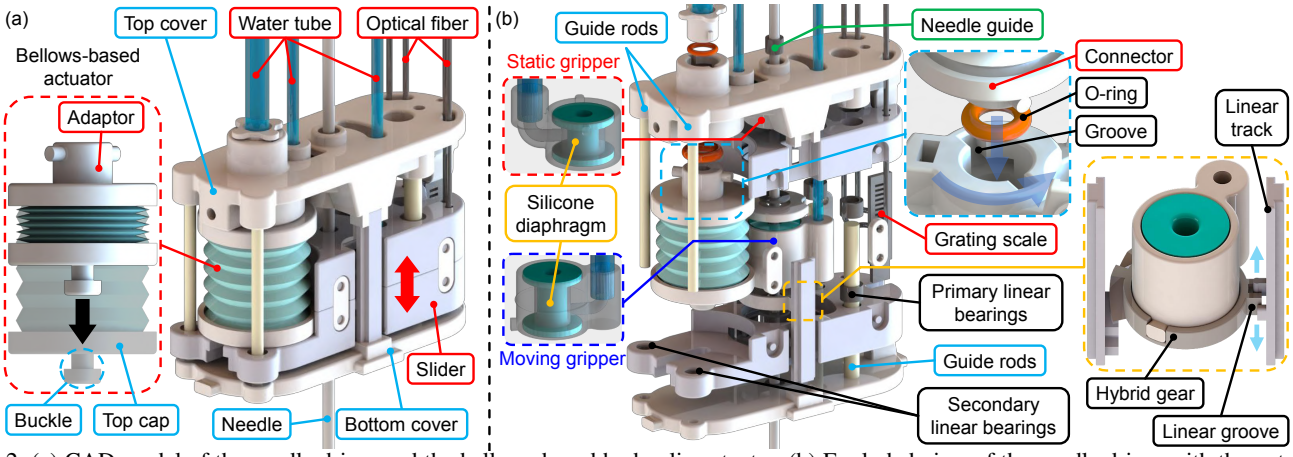

Fig. 2: (a) CAD model of the needle driver and the bellows-based hydraulic actuator. (b) Exploded view of the needle driver with the notation of each of its components.

The applied controller enables the needle driver to minimize overshoot (<0.06 mm) and achieve a repeatability error of 0.17 mm while maintaining a rapid response time. Compared to existing control methods [21], [29], [31], [32] for needle-driven systems, the proposed approach eliminates the need for precise system modeling while also avoiding reliance on higher-resolution MR-conditional encoders.

In the rest of the article, the mechanical design of the needle driver is presented in Section II. Detailed descriptions of the needle driver's components are included, and the working principle and manufacturing procedure are also introduced. Section III describes the application of the fuzzy control method in the needle driver and the corresponding control schematic. In Section IV, a prototype of the proposed needle driver is evaluated for its accuracy, repeatability, output force, and MRI-compatibility.

II. Mechanical Design

A. Design Criteria

Our objective is to develop a compact MR-safe robotic needle driver that can perform various essential needle insertion tasks in percutaneous surgical procedures, critical for facilitating clinical adoption. The needle insertion tasks could involve keeping the needle trajectory straight for optimal targeting, reducing tissue interaction force for improved puncturing performance, and performing needle steering to avoid critical anatomical obstacles. Under these consideration, the following design criteria have been identified.

1) Motion distance and motion capabilities: Considering the height of the needle positioning platform, the needle driver should be responsible for translating the needle for a distance of at least 150 mm appropriate for percutaneous procedures in most anatomical regions, including brain and torso [33], [34]. Besides linear translation, the needle driver should provide needle rotation that can potentially help minimizing needle deflection within the soft tissue, reducing tissue resistance force, and providing nonlinear steering capability.

2) Accuracy: The positioning accuracy of the needle driver in most needle-based procedures is expected to be at least 0.5 mm [29], [35], ensuring successful tissue sampling or treatment in the region of interest.

3) Size: The size of the MR scanner bore and MR imaging coil present a significant restriction to the size, in particular the height (along the needle axis direction), of the needle driver especially when it is configured in the radial direction of the bore. Considering the smallest state-of-the-art MR-safe rotatable needle driver is 33 cm in height [29] and the non-rotatable needle driver is 4 cm in height [22], our goal is to develop an MR-safe rotatable needle driver with a maximum height of 4 cm.

4) Insertion force: The force required for a needle to penetrate different tissues can vary from 1 to 10 N [36]. The needle driver should therefore provide at least 10 N insertion force. It should be noted that in gripper-based needle drivers, the needle insertion force is different from the actuator force since it depends on the contact friction between the gripper and the needle.

5) MR safety: According to the MRI compatibility standard by the American Society for Testing and Materials (ASTM) F2503-13 [37], the robotic needle driver must pose no hazard to the patient and the MR scanner. As an MR-safe robotic device, all components of the needle driver should be non-metallic, non-magnetic, and non-conductive to prevent any electromagnetic interference and ensure optimal MR image quality during its operation.

Based on the above design criteria, as shown in Fig. 1, an MR-safe needle driver actively driven by a single hydraulic bellows-based actuator has been developed. Three output motion types can be associated with the needle driver, as follows:
1) Independent needle translation without any rotation.
2) Needle translation with passive rotation. In other words, the needle rotates passively and synchronously with its translation motion.
3) Independent needle rotation. This happens by implementing motion type 1 and motion type 2 sequentially. More details can be found in Section II(E).
It measures only 2.2 cm × 5.3 cm × 3.8 cm (length × width × height), making it compact enough to be easily integrated into most robotic needle positioning platforms [5], [7], [38]. It is made entirely of MR-safe components, such as 3D printed structural and functional parts (i.e. bellows and grippers), polyurethane (PU) tubings, ceramic bearings, and

IEEE Transactions on Robotics (T-RO) paper, presented at ICRA 2026, Vienna, Austria. Cite as T-RO paper.

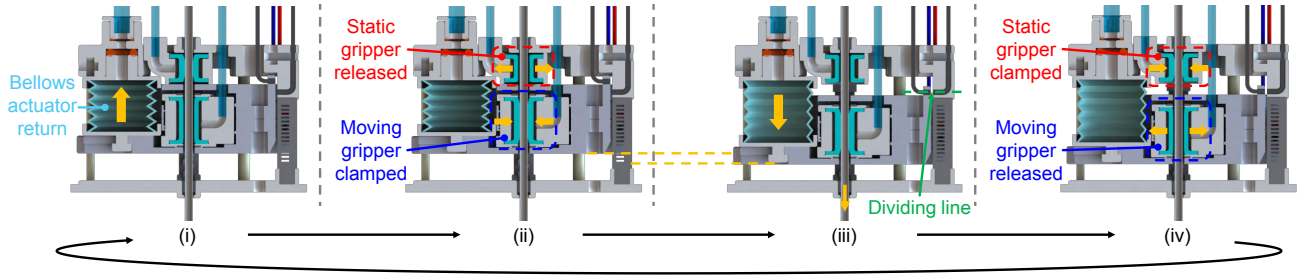

Fig. 3: Sectional view of independent needle insertion process, accomplished by the bellows actuation with sequential grip and release of the static and moving grippers. The slider starts moving from the top of the needle driver and continues until it reaches the dividing line.

optical fibers.

B. Motion Type I: Independent Needle Translation

To minimize the size of the needle driver, an inchworm motion-based mechanism was adopted in the needle driver to provide the first motion type of independent needle translation. As shown in Fig. 2, it comprises a bellows-based actuator, slider-guide system, two hydraulically activated grippers, and a grating scale for the position feedback.

*1) **Bellows-based Actuator**:* The bellows-based actuator was composed of a bellows with a cap and a connector attached to both its ends by adhesive (5400, Ergo, Switzerland). The bellows offers a high stroke-to-length ratio, thus keeping the actuator compact. It expands and contracts under hydraulic pressure control to translate the needle during its insertion and withdrawal processes. Unlike traditional piston-cylinder systems that often encounter the sealing issue, the bellows-based design ensures that the hydraulic actuator functions as a watertight system, minimizing the risk of water leakage.

As shown in Fig. 2(a), the buckle and the adapter of the bellows-based actuator are attached to the slider and the top cover of the needle driver, respectively. The water tube and bellows connectors in the top cover are designed with grooves to allow the bellows-based actuator and its corresponding water tube to be securely locked in place. Furthermore, each connector is equipped with an O-ring to ensure the system remains watertight, as shown in Fig. 2(b). Upon application of water pressure, the hydraulic actuator expands axially, propelling the slider downward. At the same time, the moving gripper, positioned at the central axis of the slider, grips the needle, and drives the needle downward to perform each needle insertion step of 2.45 mm. It should be noted that a hybrid gear, rigidly connected to the bottom of the moving gripper, features a linear groove that remains engaged with a linear track throughout its translation motion, as shown in Fig. 2(b).

*2) **Slider-guide Systems**:* Since the bellows-based actuator is mounted off the axial center of the needle driver, its movement may cause the slider to deflect from its central axis. In light of this, a combination of plastic linear bearings and ceramic guide rods have been added to ensure smooth vertical movement of the slider during actuation of the bellows.

As shown in Fig. 2(b), the slider contains four linear bearings that are divided into two pairs of primary and secondary linear bearings. Each primary linear bearing has an outer diameter of 5.5 mm and an inner diameter of 4 mm, with two 4 mm ceramic rods acting as its guide. The primary linear bearings are placed between the moving gripper and the encoder, serving as the main support for the slider. When the bellows-based actuator are placed eccentrically, it causes extra torque on the primary bearings, resulting in increased resistance on the opposite side of the slider, which affects its smooth movement. Therefore, a pair of secondary linear bearings are incorporated on the opposing side to achieve force equilibrium on the slider. The secondary linear bearings have an outer diameter of 3.5 mm and an inner diameter of 2 mm and are guided by two 2 mm ceramic rods as their guide rails. To achieve a more compact design, the guide rails are snugly fitted against the bellows to minimize space occupation.

Needle guides are also designed to prevent the needle from getting skewed in the needle driver. They are made of medical-grade peek material to ensure biocompatibility. As illustrated in Fig. 2(b), they are inserted in two apertures located at the proximal and distal ends of the needle driver. Linear bearings with an outer diameter of 3.5 mm and an inner diameter of 2 mm were adopted as the needle guides. These parameters can be changed to match the actual diameter of the needle.

Working Sequence: The needle driver employs the grip-move-release working sequence, as shown in Fig. 3, to achieve step-by-step needle insertion. The slider starts at the top cover of the needle driver, and moves between the top cover of the needle driver and the dividing line to perform independent needle insertion process. The working sequences mainly include the following four steps:

Step (i): The bellows-based actuator is actuated to pull the moving gripper upwards to return to the starting point while the static gripper holds the needle;

Step (ii): The static gripper releases the needle, while the moving gripper clamps its grip;

Step (iii): The bellows-based actuator is actuated to push the moving gripper, and thus the needle downwards to drive the needle insertion process.

Step (iv): The moving gripper releases the needle at its endpoint, while the static gripper firmly clamps it to ensure that the needle remains stationary despite the slider's motion.

These four steps constitute a single cycle that drives the needle downwards. This cycle can be repeated infinitely to insert the needle for any desired depth. Conversely, when executed in the reverse direction, the cycle results in needle withdrawal.

C. Motion Type II: Needle Translation with Passive Rotation

Integrating an additional degree of freedom (DOF) of active needle rotation typically requires an additional actuator. To

IEEE Transactions on Robotics (T-RO) paper, presented at ICRA 2026, Vienna, Austria. Cite as T-RO paper.

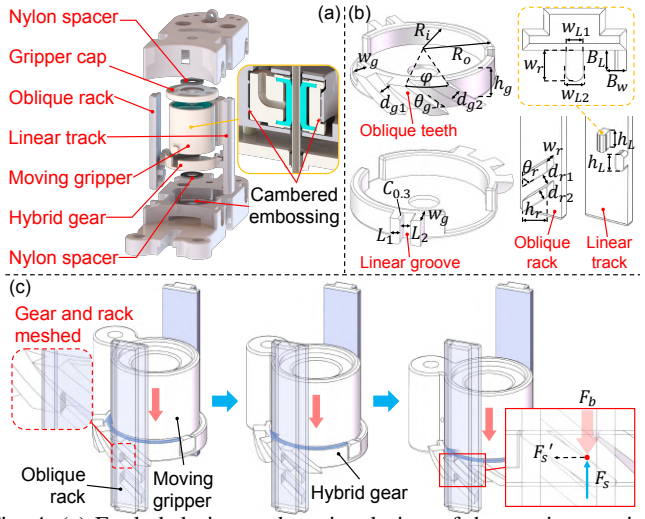

Fig. 4: (a) Exploded view and sectional view of the passive rotation mechanism. (b) CAD schematics of the hybrid gear with oblique teeth and linear groove, oblique rack and linear track. C0.3 indicates a chamfer of 0.3 mm. (c) Rotation process of the passive rotation mechanism.

maintain the compactness of the needle driver, we instead introduce a passive needle rotation mechanism that moves synchronously with the active needle insertion mechanism. It should be recognized that excessive needle rotational velocity may cause significant pain and soft tissue damage [39]. However, reducing tissue resistance and keeping needle trajectory straight with minimal deflection does not require high rotational speed [25]. So, a linear-to-rotary motion ratio of 1 mm to 10 degrees was tentatively adopted in the passive needle rotation mechanism. It can be changed according to the actual clinical requirements.

As shown in Fig. 4(a), the slider consists of a nylon spacer, gripper cap, moving gripper, and hybrid gears arranged in sequence, preventing any relative axial displacement of the moving gripper within the slider. An oblique rack is rigidly attached to the top and bottom covers of the slider and placed opposite to the linear track. The hybrid gear features oblique teeth configured in perpendicular to the oblique rack, and is free to rotate and move axially.

TABLE I: Robot design parameters

Parameter	Value	Parameter	Value
w_g	1.5 mm	w_r	1.5 mm
d_{g1}	1.31 mm	d_{r1}	1.29 mm
d_{g2}	1.0 mm	d_{r2}	1.0 mm
θ_g	45 °	θ_r	45 °
φ	30 °	L	3 mm
h_g	3 mm	h_r	3 mm
R_i	6 mm	R_o	7 mm

The detailed parameters of the hybrid gear are shown in Fig. 4(b) and table I. The linear-to-rotary motion ratio δ of the needle driver can be determined by the ratio of the tooth height of the hybrid gear h_g to the angular pitch φ, as expressed by:

$$\delta = \frac{h_g}{\varphi} \tag{1}$$

The tooth width of the hybrid gear (d_{g2}) and rack (d_{r2}) are two critical parameters of the mechanism and are set as 1 mm to prevent manufacture failure and ensure robust mechanical properties. Other parameters are determined based on the desired linear-to-rotary motion ratio, fundamental geometric relationships, and empirically derived manufacturing tolerances. During needle insertion, a downward force from the hydraulic bellows-based actuator F_b (the red arrow in Fig. 4(c)) is applied to the hybrid gear. The oblique rack generates an equal and opposite supporting force F_s (the blue arrow in the figure). This supporting force creates a tangential force F_s' (the black arrow in the figure) on the hybrid gear through its bevel teeth, thereby causing the moving gripper and the needle to rotate passively during the needle translation. With a 45° tooth interface, this rotation stems from the force decomposition at the teeth, leading to the following force-torque transfer efficiency:

$$\eta = \frac{\cos(45^\circ)}{1+\sin(45^\circ)} \approx \frac{\sqrt{2}}{2} \approx 70.7\%.$$

The nylon spacer is positioned above the top cap of the moving gripper and below the hybrid gear to minimize friction during its rotation. During its rotation, any undesired radial translation is limited by the cambered embossing, designed to be semi-circular to minimize the contact surface and thus reduce friction.

Working Sequence: Needle translation with passive rotation utilizes the same grip-move-release working sequence as the independent needle translation previously described in section B 3), except the different starting and ending points. As depicted in fig. 5, the slider starts at the dividing line, and moves between the dividing line and the bottom cover of the needle driver to perform passive rotary needle insertion process.

D. Motion Decoupling and Switching between Motion Types I and II

*1) **Principle of Motion Decoupling**:* The full stroke of the needle driver can be divided into two distinct parts separated by the dividing line, as shown in Fig. 6(a) with the upper part covering the independent translation motion and the lower part covering the translation with passive rotation. The motion type stays the same if the slider moves back and forth within the upper part or the lower part without passing the dividing line. The hybrid gear is designed in such a way that its linear groove decouples from the linear track and its oblique teeth engages with the oblique rack at the instant the hydraulic bellows-based actuator pushes the slider downwards past the dividing line, transitioning the output motion from independent needle translation to needle translation with passive rotation and thus completing the motion decoupling. Conversely, when the slider moves upwards past the dividing line, the vertical groove will be obstructed by the stopper on the linear track, and then the

IEEE Transactions on Robotics (T-RO) paper, presented at ICRA 2026, Vienna, Austria. Cite as T-RO paper.

output motion will reverse direction to achieve the motion decoupling.

*2) **Sensor-based Motion Switching**:* A fiber optics-based sensing system has been designed to provide real-time position and state feedback, enabling closed-loop control of both independent translation motion and translation with passive rotation motion of the needle driver. The sensing system consists of an incremental AB-phase encoder, a static fiber, and a sliding fiber. A switching signal transmits between the static and sliding fibers, indicating whether the current motion type of the needle driver is independent translation or translation with passive rotation.

As seen in Fig. 6(b), three emitting fibers (QiYi, QY40-1.0E, China) were connected to the laser light sources to generate A phase, B phase and switching signals. The A phase fiber and B phase fiber are attached to the slider of the needle driver. The AB phase encoder signals propagate between the emitting and receiving fibers via an acrylic grating scale with a 0.5 mm spacing distance, providing relative motion amplitude and motion direction information. This spacing is empirically determined by the machining precision, the loss of light during propagation, and sensitivity of the photodiode module (TELESKY, Photodiode, China). Then, the photodiode modules connected to the receiving fibers convert these light signals into corresponding electrical signals for recording.

The incorporation of static and sliding fibers not only facilitates recognition of the needle driver's current motion type, but also can reduce its cumulative positioning error. The static fiber always remains fixed on the needle driver, while the sliding fiber is attached to and free to move with the slider. As shown in Fig. 6(b), unlike the AB phase encoder signals, the switching signal propagates between the static and sliding fibers directly, without passing through the grids of the grating scale. When the static fiber aligns with the sliding fiber at the dividing line, a switching signal is generated to indicate the switching from one motion type to the other. In addition to identifying motion type, this switching signal also serves as a position reference. By providing an absolute positional reference at a predefined point in the slider's travel, the switching signal enables correction of cumulative positioning errors that arise during each motion cycle.

E. Motion Type III: Independent Needle Rotation

Switching signals provided by the sensing system accurately indicate the current motion type of the needle driver, enabling the sequential implementation of the two aforementioned motion types to achieve a third motion type: independent needle rotation. Essentially, the needle is first retracted by a predetermined distance using the independent translation motion. This retraction serves as a critical compensatory function, accounting for the distance the needle travels during its subsequent forward translation with passive rotation, making the needle perform effectively only rotational motion.

Working Sequence: The sectional view of the needle driver is shown in Fig. 7 and the working sequences mainly include the following eight steps:

Step (i): The bellows-based actuator is actuated to pull the moving gripper back to the dividing line, while the static gripper holds the needle;

Step (ii): The static gripper releases the needle at the dividing line, while the moving gripper clamps its grip;

Step (iii): The bellows-based actuator is actuated to pull the moving gripper upward by a certain distance, and thus the needle is retracted.

Step (iv): The moving gripper releases the needle, while the static gripper clamps its grip, ensuring that the needle will not move with the slider's motion.

Step (v): The bellows-based actuator is actuated to push the moving gripper downwards until a switching signal is generated, while the needle stays static under the effect of the clamped static gripper.

Step (vi): The static gripper releases the needle at the dividing line, while the moving gripper clamps its grip.

Step (vii): The bellows-based actuator is actuated to push the moving gripper downward by the same distance as in step (iii), and thus the needle moves downwards with passive rotation. Since the downward movement of the needle is compensated by the upward movement in (iii), the needle realizes a pure rotational motion compared to the initial state (i).

Step (viii): The moving gripper releases the needle, while the static gripper clamps its grip, ensuring that the needle will not move with the slider's motion.

These eight steps constitute a single cycle that drives the needle to rotate at an angle of 10 times the linear motion distance. This cycle can be repeated infinitely to rotate the needle for any desired angle.

F. Needle Gripper

Each hydraulics-activated needle gripper comprises a cylindrical silicone diaphragm and an ABS housing, bonded together using adhesive (GuPai, Silicone adhesive, China). As

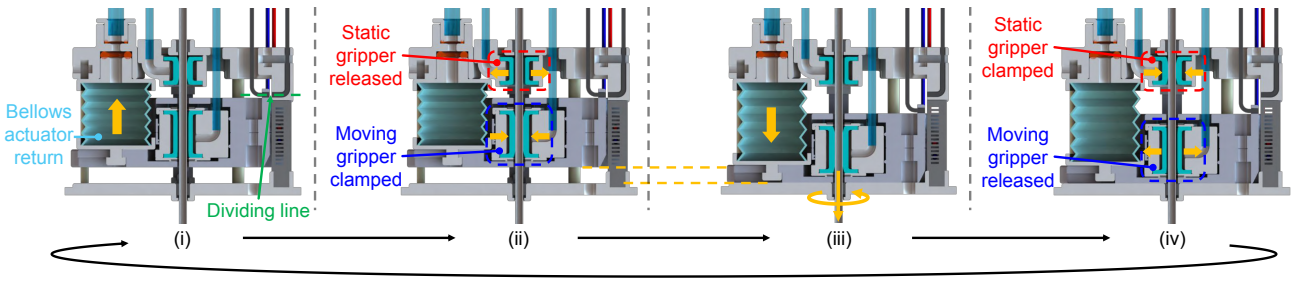

Fig. 5: Sectional view of the needle insertion with passive rotation process, accomplished by the bellows actuation with sequential grip and release of the static and moving grippers. The slider starts moving from the dividing line and continues until it reaches the bottom of the needle driver.

IEEE Transactions on Robotics (T-RO) paper, presented at ICRA 2026, Vienna, Austria. Cite as T-RO paper.

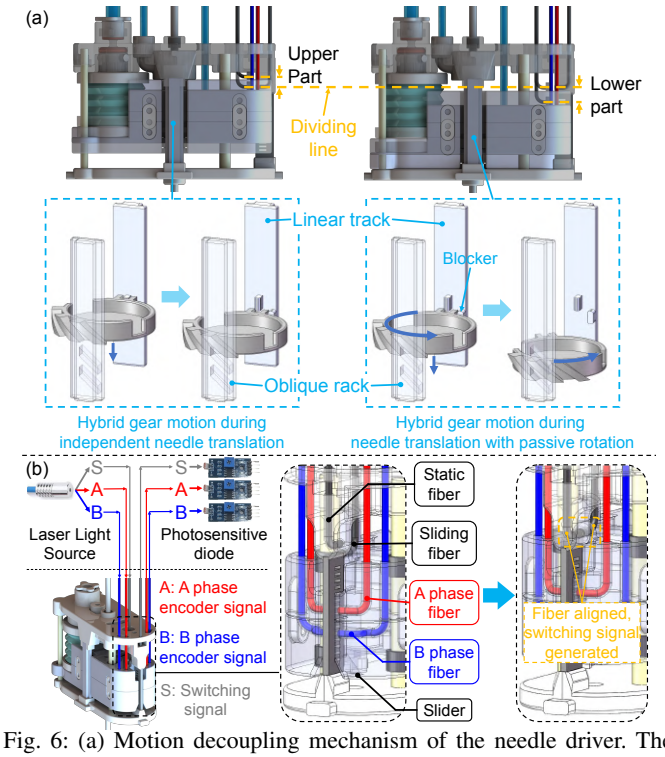

Fig. 6: (a) Motion decoupling mechanism of the needle driver. The hybrid gear engages with the linear track for independent translation in the upper part of the stroke above the dividing line and engages with the oblique rack for translation with passive rotation in the lower part of the stroke below the dividing line. (b) Illustration of the sensing system, including the fiber optics-based AB phase encoder, the static fiber, and the sliding fiber.

shown in Fig. 8, silicone diaphragm A is used as the static gripper to hold firmly the needle during the retraction of the slider. The inner diameter of silicone diaphragm A is designed to be 1 mm larger than the needle diameter, allowing the needle to pass through smoothly during every needle insertion step. When positive pressure is applied, the inner wall of silicone diaphragm A shrinks and clamps the needle.

Compared to the static gripper, the moving gripper requires a higher clamping force to overcome tissue resistance during needle insertion. Increasing the contact area between the silicone diaphragm and the needle can increase the clamping force of the gripper. Silicone diaphragm B1 was proposed by doubling the height of silicone diaphragm A to 10 mm. However, the finite element analysis (FEA) results in Fig. 8(b) illustrate that silicone diaphragm B1 shrinks irregularly under positive pressure, similar to silicone diaphragm A. The uneven shrinkage over the longer diaphragm body significantly reduces the effective contact area between the needle and the silicone diaphragm, resulting in reduced clamping force. To prevent the silicone film from shrinking irregularly under positive pressure, a pre-clamped silicone diaphragm design (i.e diaphragm B2) was proposed by maintaining its height at 10 mm and reducing its inner diameter to 2 mm to match the needle diameter. The pre-clamping design allows silicone diaphragm B2 to securely hold the needle under positive pressure without irregular shrinkage. However, it does not release the needle under negative pressure, as shown by the FEA-simulated cross section of silicone diaphragm B2 in Fig. 8(b). Finally, silicone diaphragm B3 was proposed and selected as the final design for the moving gripper. Besides retaining the pre-clamped design from B2, it features a 15° fillet at the top and bottom edges of the lumen. This new design not only eliminates uneven shrinkage and offers a high clamping force under positive pressure, but also offers sufficient expansion to properly release the needle under negative pressure.

Fig. 9(a) illustrates the detailed compression molding procedure of the proposed silicone diaphragms, which have a Shore hardness of 40 A. Firstly, we mix and stir liquid silicone A and B well before using a vacuum to remove air bubbles from the mixture. Mold A and mold B are prepared to fabricate silicone diaphragm A and B, which are used as the static and moving gripper respectively. In each mold, the container is assembled first before the silicone mixture is poured into it. It is then sealed with a pillar, and covered with the top and bottom caps. After the silicone mixture solidifies, the silicone diaphragms can be obtained by splitting the molds, as shown in Fig. 9(b).

III. Controller Design

A. Hydraulic Teleoperation System

To control the robotic needle driver, a master-follower teleoperation system is employed with water as the transmission medium between the master side in the MR control room and the follower side (i.e. needle driver) in the MR scanner. As shown in Fig. 10, the master side consists of motorized syringes, a microprogramming control unit (MCU), and an optical transceiver module. The bellows-based actuator, the static gripper and the moving gripper of the needle driver are connected to their respective syringes on the master side through long polyurethane (PU) tubes.

The syringe connected to the bellows-based actuator is driven by a motorized ball screw module, facilitating continuous linear displacement of the bellows. As seen in Fig. 10, the syringe piston is rigidly connected to the ball screw slider, while the syringe cylinder is rigidly connected to the base. Driving the ball screw directly causes displacement in the syringe piston, which in turn generates positive or negative pressure changes to control the expansion and contraction of the bellows. In contrast to the bellows-based actuator, which is required to produce smooth and continuous movement, the needle grippers have only two states: open and closed. Compared with ball screws, which require 1–2 s for equivalent motion due to mechanical inertia, pneumatic cylinders were used to actuate the gripper syringes because they achieve full extension/retraction in approximately 0.3 s. STM32 (STMicroelectronics, STM32F407, Italy) was used as the MCU of the robotic system. It regulates the motor speed and the status of the grippers based on the feedback signal from the encoder, to achieve closed-loop position control of the needle.

B. Filtered Observer-Based Adaptive Elastic Fuzzy Controller

In the teleoperation control architecture involving long hydraulic tubings, liquid damping introduces significant hysteresis effects, adversely affecting the system's response characteristics. Additionally, the internal mechanical transmission

IEEE Transactions on Robotics (T-RO) paper, presented at ICRA 2026, Vienna, Austria. Cite as T-RO paper.

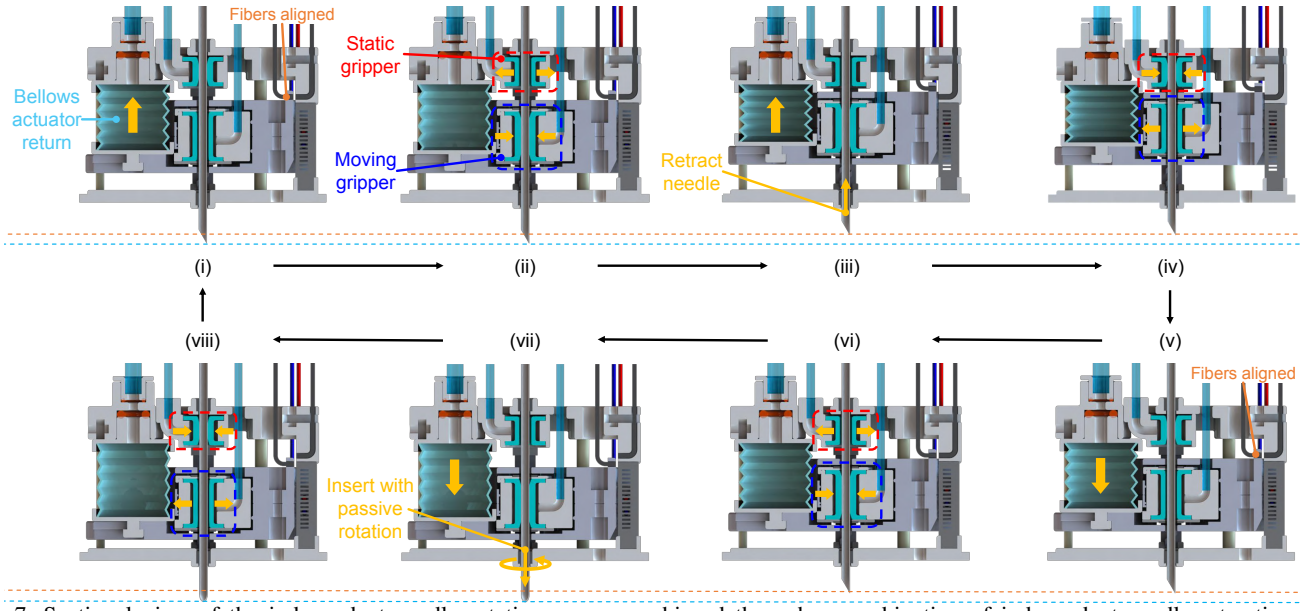

Fig. 7: Sectional view of the independent needle rotation process, achieved through a combination of independent needle retraction and needle insertion with passive rotation.

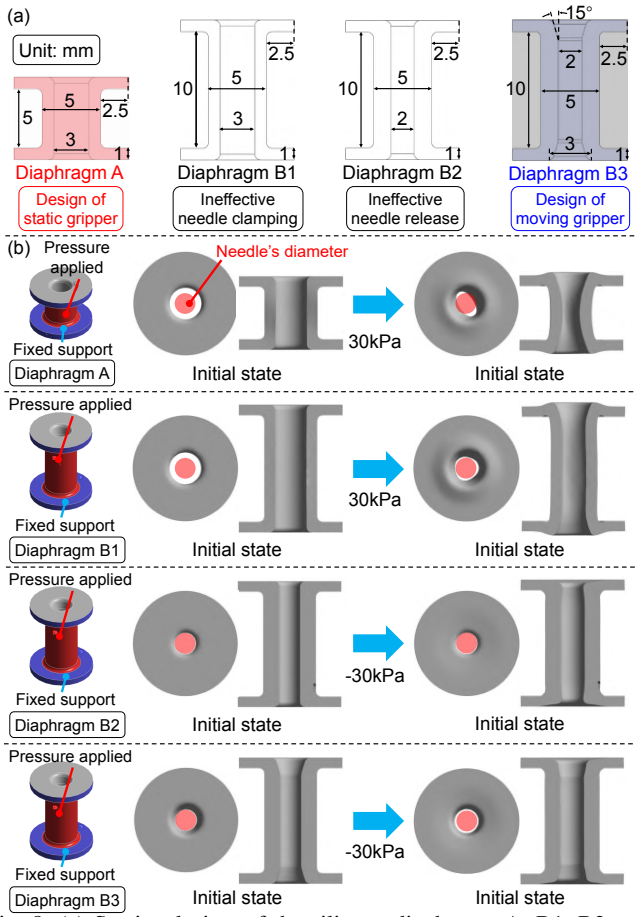

Fig. 8: (a) Sectional view of the silicone diaphragm A, B1, B2, and B3. The silicone diaphragm A and B3 were selected as the static and moving grippers, respectively. (b) FEA results of the silicone diaphragm A, B1, B2, and B3. The red circle indicate the needle's diameter.

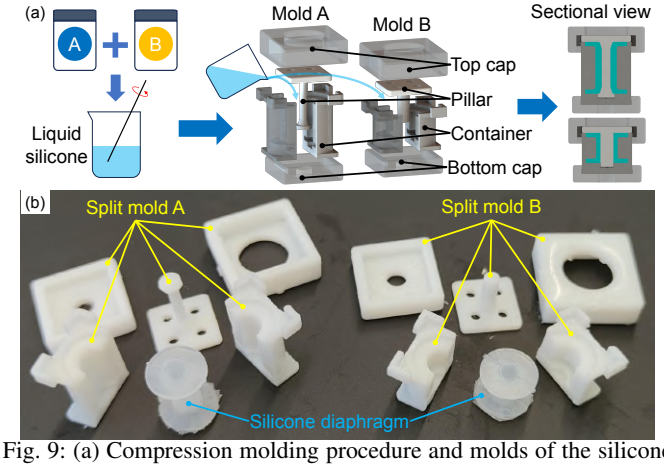

Fig. 9: (a) Compression molding procedure and molds of the silicone diaphragms. (b) Actual result of the split molds and finished silicone diaphragms.

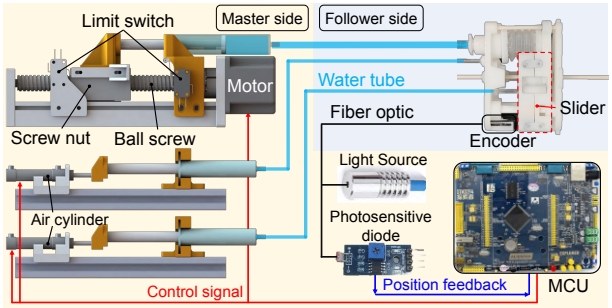

Fig. 10: Illustration showing the hydraulic teleoperation system of the needle driver. The orange part indicates the master side of the system, which is located outside the MR room. The blue part indicates the follower side (i.e. the needle driver) of the system, which is located in the MR scanner.

structures of the needle driver introduce time-varying friction, which results in uncertain dead-zone characteristics during the operation of the bellows-based actuator. All these introduce nonlinear factors in the system dynamics, which is difficult to model and makes accurate control of the needle driver highly challenging. Besides, even though the master-side stepper motor can achieve high motion precision, the fiber optic encoder in the follower-side needle driver has a resolution of only 0.5 mm due to the machining limitation, limiting state feedback to discrete steps. This limitation introduces quantization errors in the state estimation and increases measurement noise, making it challenging to accurately reconstruct the follower-side state and potentially degrading overall control performance.

The proportion-integration-differentiation (PID) controller has been widely adopted in many MR-safe surgical robotic systems [31], [40]. However, the PID controller struggles to effectively control the hydrostatic bellows-based needle driver due to its limitations in handling dead-zone nonlinearity, hysteresis effects, and uncertain varying friction, making it difficult to ensure stability and dynamic performance, and even leading to chattering. Different from PID control, sliding mode control (SMC) [21], [29], [32] offers stronger robustness against uncertain friction, but it relies heavily on accurate system modeling, which makes it difficult to apply to the proposed needle driver with unknown nonlinear dynamics. To achieve accurate, stable control of the needle driver and mitigate motion chattering when approaching the target, a filtered observer-based adaptive elastic fuzzy (FO-AEF) controller is introduced in this work.

Compared with conventional controllers such as PID, which struggle with dynamic uncertainties, varying dead-zone nonlinearities, hysteresis, and limited sensor resolution, the FO-AEF controller leverages a novel adaptive elastic fuzzy logic and filter-based observer to address these challenges more effectively. It simplifies complex system behavior by partitioning it into multiple fuzzy sets using IF-THEN rules, enabling adaptation to varying system dynamics. Specifically, the FO-AEF controller dynamically adjusts the scaling, center, and sharpness of its membership functions in real time, enabling precise adaptation to varying operating conditions. This elasticity in membership function parameters enhances robustness and reduces sensitivity to system variations, which represents a significant improvement over traditional fuzzy controllers. Additionally, a high-gain observer integrated with a low pass filter is designed to estimate the true states, effectively eliminating quantization noise. These mechanisms allow the FO-AEF controller to maintain stable, smooth, and accurate needle motion, even in the presence of hysteresis, varying dead-zone and unknown dynamics.

The proposed needle driver control strategy is illustrated in Fig. 11. In this system, it is assumed that the needle and the slider are rigidly connected, and the bellows-based actuator is considered as a hydraulic cylinder coupled with a spring-damping system. Similarly, the hydrodynamics of the entire hydraulic line are also considered as an equivalent spring-damping system. The following notations are used in the analysis hereafter:

- M_s: The overall mass.
- P_1, A_1: Pressure and cross-sectional area of the hydraulic cylinder on the master side, respectively.
- P_2, A_2: Pressure and cross-sectional area of the bellows-based actuator on the follower side, respectively.
- c_w, k_w: Equivalent damping and stiffness of the water, respectively.
- c_b, k_b: Equivalent damping and stiffness of the bellows-based actuator, respectively.
- F_f: Unknown varying friction force.
- u: Displacement of the master side screw nuts.
- x_b: Displacement of the needle.
- y: Measurement of x_b from the integrated encoder with a resolution of 0.5 mm.

The dynamic equation of the system can then be described as:

$$M_s\ddot{x}_b = P_2(u, c_w, k_w, t)A_2 - c_b(\dot{x}_b, t)\dot{x}_b - k_b(x_b, t)x_b - F_f \quad (2)$$

Define the system state as $x = [\ x_1 \quad x_2\ ]^{\mathrm{T}} = [\ x_b \quad \dot{x}_b\ ]^{\mathrm{T}}$ and the control input as $u = u_s$. The state-space representation of (2) can then be expressed as

$$\begin{cases} \dot{x}_1 = x_2 \\ \dot{x}_2 = f(x,u) + \delta \\ y = x_1 + \vartheta \end{cases} \quad (3)$$

where $f(x,u) = P_2(u, c_w, k_w, t)A_2/M_s - c_b(\dot{x}_b, t)\dot{x}_b/M_s - k_b(x_b, t)x_b/M_s$ is the unknown nonlinear dynamic function, $\delta = -F_f/M_s$ represents the unknown disturbance caused by varying friction, y is the encoder measurement, and ϑ denotes the measurement noise.

A low-pass filter is used to mitigate the effects of quantization noise due to the limited encoder resolution and a high-gain observer is integrated to ensure fast convergence of estimated states to true states. The filter and observer dynamics are described by the following equations:

$$\begin{cases} \tau\dot{y}_f + y_f = y \\ \dot{\hat{x}}_1 = \hat{x}_2 + \frac{l_1}{\varepsilon}(y_f - \hat{x}_1) \\ \dot{\hat{x}}_2 = \frac{l_2}{\varepsilon^2}(y_f - \hat{x}_1) \end{cases} \quad (4)$$

where $\hat{x} = [\ \hat{x}_1 \quad \hat{x}_2\ ]^{\mathrm{T}}$ is the estimation of the system state $x = [\ x_1 \quad x_2\ ]^{\mathrm{T}}$, τ is the time constant of the low-pass filter, and l_1, l_2 are positive observer gains that must be selected to ensure stability. The parameter ε is a small but not excessively small positive parameter chosen to avoid amplifying quantization noise. The process works by first applying a low-pass filter to attenuate the high-frequency quantization noise ϑ present in the measurement y to generate a smoothed signal y_f. The time constant τ determines the level of smoothing applied to the quantized measurement y. Then, a high-gain observer uses the smoothed signal y_f to estimate the state x_b. The error dynamics of this estimation are governed by the design parameters l_1, l_2, and ε. The observer gains l_1 and l_2 ensure stable and fast error convergence by placing the observer poles to achieve suitable damping and bandwidth (for example, $l_1 = 2$, $l_2 = 1$), with the ratio l_1/l_2 maintained between 2 and 4 to prevent excessive overshoot. The parameter ε typically ranges from 0.05 to 0.5 (often set to 0.1) to balance estimation accuracy and robustness against quantization noise. A smaller ε increases convergence

IEEE Transactions on Robotics (T-RO) paper, presented at ICRA 2026, Vienna, Austria. Cite as T-RO paper.

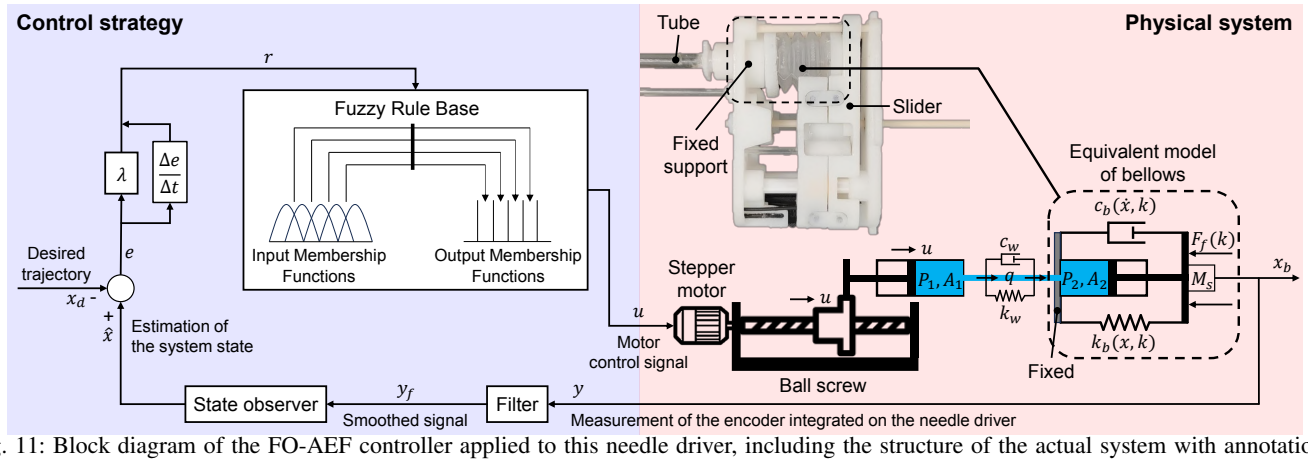

Fig. 11: Block diagram of the FO-AEF controller applied to this needle driver, including the structure of the actual system with annotations.

speed and reduces steady-state error but may amplify high-frequency noise, while a larger ε improves noise rejection but results in a slower response. By carefully tuning these parameters, the system ensures that the estimated $\hat{x}$ converges to the true value of x with the desired level of accuracy, even in the presence of quantization noise in the measurements.

Consider the expected state of the needle-driven system as x_d. Then, the tracking error reflecting discrepancies in needle placement relative to the target tissue area is defined as $e = \hat{x} - x_d$. For the tracking control of needle driver system (3), we design the following fuzzy control rules to ensure accurate needle positioning:

Rule l: **IF** ϖ_1 is F_1^l, ϖ_2 is F_2^l, $\cdots$, and ϖ_n is F_n^l
THEN $u_f^l = -K^l r$

where $l = 1, \cdots, N$ is the number of the rules, $\varpi_i (i = 1, 2, \cdots, n)$ are premise variables that are related to $\hat{x}$, $F_i^l (i = 1, 2, \cdots, n)$ are the predefined fuzzy sets, $r = \dot{e} + \lambda e$ with λ being a positive constant. By using $\mu_{F_i^l}$ to represent the fuzzy membership functions of F_i^l, we can obtain the overall output of the fuzzy logic system (FLS) as:

$$u_f = \frac{\sum_{l=1}^{N} \left(\prod_{i=1}^{n} \mu_{F_i^l}(\varpi_i) \right) K^l r}{\sum_{l=1}^{N} \left(\prod_{i=1}^{n} \mu_{F_i^l}(\varpi_i) \right)} = \sum_{l=1}^{N} \sigma^l K^l r \tag{5}$$

The fuzzy basis function is $\sigma^l = \prod_{i=1}^{n} \mu_{F_i^l}(\varpi_i) / \sum_{l=1}^{N} \left(\prod_{i=1}^{n} \mu_{F_i^l}(\varpi_i) \right)$. By denoting $K = \left[K^1, K^2, \cdots, K^N \right]^\top$ and $\sigma(\varpi) = \left[\sigma^1, \sigma^2, \ldots, \sigma^N \right]^\top$, (5) can be rewritten as

$$u_f = K^{\mathrm{T}} \sigma(\varpi) r \tag{6}$$

The selection of appropriate membership functions is important for system robustness. Considering that the unknown disturbances can cause fluctuations in hydraulic actuation signals, our fuzzy controller requires membership functions that adapt to varying inputs, thereby enhancing system resilience to unmodeled changes in the system dynamics. To the end, we use the following elastic membership function to enhance the adaptability to the unpredictable dynamics and disturbance:

$$\mu_{F_i^l}(\varpi_i) = \left[\frac{\cos^2(\alpha(\varpi_i - \beta))}{1 + \alpha^2(\varpi_i - \beta)} \right]^{\gamma^2} \tag{7}$$

Defined by parameters α, β, and γ, it provides real-time control over the scaling, center and sharpness of the function. The scaling parameter α adjusts sensitivity to input changes, the center parameter β shifts the function to align with changing operating points, and the sharpness parameter γ controls the tolerance to noise or disturbances. This elasticity allows the membership function to adapt to varying inputs, ensuring effective rule evaluations and stable performance in systems with nonlinearities or time-varying dynamics, especially when the needle interacting with tissues of varying stiffness. In section A1 of appendix, we have included specific examples illustrating how these parameters are dynamically adjusted during needle insertion process.

In the control procedure, the gradient descent based tuning laws for FLS are determined by

$$\nabla K = W_K(\mu_{F_i^l} - \alpha X - \beta Y - \gamma Z) r^{\mathrm{T}} - k_K W_K \|r\| \tag{8}$$

$$\nabla \alpha = W_\alpha X^{\mathrm{T}} K r - k_\alpha \alpha W_\alpha \|r\| \tag{9}$$

$$\nabla \beta = W_\beta Y^{\mathrm{T}} K r - k_\beta \beta W_\beta \|r\| \tag{10}$$

$$\nabla \gamma = W_\gamma Z^{\mathrm{T}} K r - k_\gamma \gamma W_\gamma \|r\| \tag{11}$$

where $k_K, k_\alpha, k_\beta, k_\gamma$ are regularization terms, $W_K, W_\alpha, W_\beta, W_\gamma$ are designed parameter matrices, and $X = \partial \mu_{F_i^l} / \partial \alpha, Y = \partial \mu_{F_i^l} / \partial \beta, Z = \partial \mu_{F_i^l} / \partial \gamma$ are Jacobian matrices. The gradient descent-based update laws dynamically tune the parameters K, α, β, and γ to minimize the control error r, ensuring the membership function remains optimized for the current system state. Each update uses the sensitivity of the membership function X, Y and Z to guide adjustments, while regularization terms prevent excessive or abrupt changes that could destabilize the system. The error-driven updates enable real-time adaptation and allows the fuzzy controller to continuously adjust to disturbances or shifts in dynamics while maintaining stability and precision.

IV. Experimental Study

A. Tracking Evaluation during Needle Translation

The position tracking capabilities of the needle driver operating under the proposed control framework were evaluated using the experimental platform shown in Fig. 12. An electromagnetic (EM) sensor (Aurora Micro 6DOF Sensor, NDI,

Canada) was enveloped by a 3D printed component and affixed to the needle tip for real-time data collection. Supplementary experiments in section A2 of appendix comparing the EM sensor to a high-precision linear encoder (OID, R274096, China) with 0.05 mm resolution yielded an RMS error of 0.04 mm and a maximum error of 0.48 mm. These results confirm the sensor's reliability, showing low variance in repeated trials and ensuring that the reported metrics accurately reflect true needle driver performance. In the tracking evaluation, some air was retained in the hydraulic lines to amplify control challenges and more effectively highlight the performance differences between the controllers. During the experiments, the needle was controlled to follow the reference step signal shown in Fig. 13(a) using the reading of the fiber optic encoders as feedback. The experimental results under the PID and the FO-AEF controllers are measured by the EM-sensor and shown in Fig. 13. The FO-AEF controller's mean and maximum steady-state errors are 0.2 mm and 0.48 mm, which are over 58% lower than the PID controller's mean and maximum steady-state errors of 0.48 mm and 0.92 mm. The high-gain observer enables FO-AEF to reduce the steady-state errors caused by sensor quantization errors caused by the low-resolution fiber optic sensor feedback. Furthermore, as the robotic needle approaches the target under the PID controller, the system's hysteresis causes the actual response to lag behind changes in the control signal, resulting in overshoot. The same hysteresis effect, when the error reverses, leads to excessive correction of the control input. Combined with dead-zone nonlinearity and sensor quantization errors, it ultimately causes chattering during the low-speed motion. Compared to the PID controller, which has an average overshoot of 1.96 mm, the FO-AEF controller achieves negligible overshoot (<0.06 mm) while responding faster. This is primarily attributed to the elastic membership functions in the FO-AEF controller, which can dynamically adjust control gains in the low-speed motion, thereby suppressing overshoot and chattering.

In addition to the step signals, the needle was controlled to track a reference sinusoidal signal shown in Fig. 14(a), with the corresponding data recorded by the EM sensor, under the FO-AEF, PID, and learning-based controller using Bayesian optimization (BO) [41], respectively. The limitations of the PID controller become more pronounced in situations that require precise and rapid adjustments, where frequent changes in motion and direction make the effects of hysteresis and dead-zone nonlinearity even more noticeable. Similarly, the BO controller, while better than PID, still lags behind the reference signal and struggles to maintain accuracy during rapid motion changes, as seen in the figure. In contrast, the adaptive gain adjustment and robustness to quantization noise of the FO-AEF controller allow it to achieve significantly smoother and more accurate sinusoidal tracking compared to the PID controller. Based on the evaluation, the FO-AEF controller achieves a mean tracking error of 0.23 mm and a maximum tracking error of 0.99 mm. In comparison, the PID controller's mean and maximum tracking errors are 1.11 mm and 4.31 mm, respectively, while the BO controller's errors are 0.62 mm and 2.2 mm. These results further validate the superiority of the proposed FO-AEF controller in enabling accurate tracking of continuous bidirectional trajectories with minimal deviation.

To elucidate error characteristics, we differentiate between dynamic tracking errors in sinusoidal signals and steady-state errors in step responses. The 0.99 mm maximum error in sinusoidal tracking (0.1 Hz, 5 mm amplitude) stems mainly from phase lag due to hydraulic damping and hysteresis in the teleoperation system, evident during rapid direction changes. Conversely, steady-state errors for step signals remain below 0.48 mm, demonstrating robust performance in quasi-static needle placement tasks.

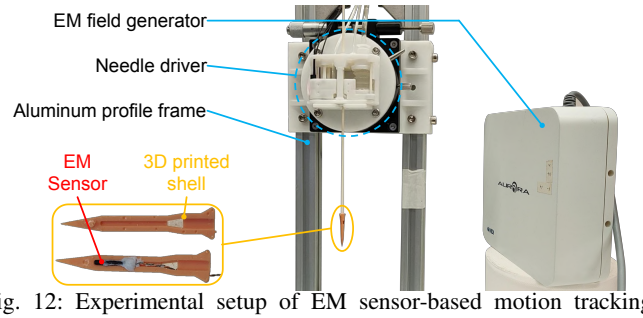

Fig. 12: Experimental setup of EM sensor-based motion tracking evaluation. A needle driver was attached to a rotating platform, which was then mounted on an aluminum profile frame.

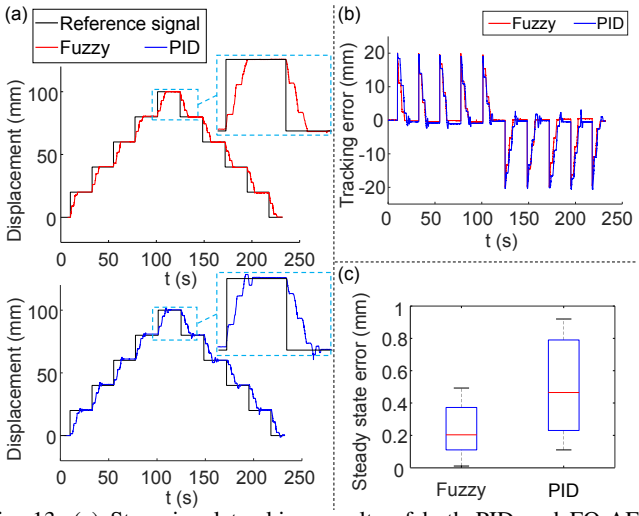

Fig. 13: (a) Step signal tracking results of both PID and FO-AEF controller. (b) Tracking errors of both PID and FO-AEF controller. (c) Boxplot graphs of the steady-state error of both PID and FO-AEF controller.

B. Repeatability Evaluation of Needle Translation and Rotation Motions

During the repeatability evaluation experiments, the needle driver was programmed to repeatedly translate the needle under motion type II between 0 and 10 mm using the same experimental setup shown in Fig. 12. The passive rotation mechanism rotates the needle from 0 to 100° as it moves from 0 to 10 mm, according to the proposed linear-to-rotary motion ratio δ. The EM sensor attached to the needle's tip recorded the needle's distance traveled and angle of rotation, as shown in Fig. 15(a).

IEEE Transactions on Robotics (T-RO) paper, presented at ICRA 2026, Vienna, Austria. Cite as T-RO paper.

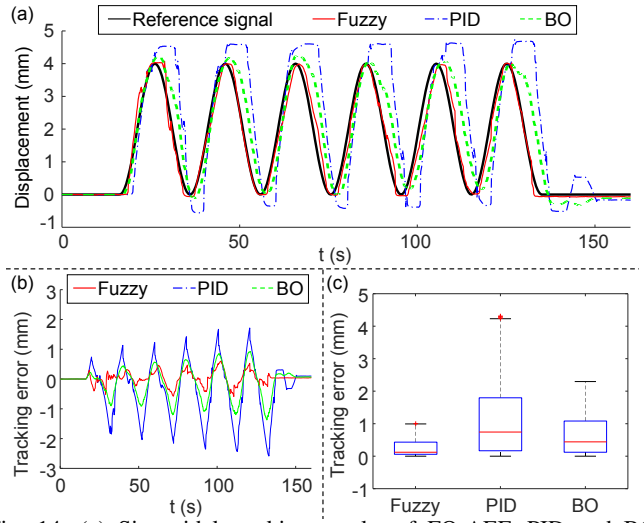

Fig. 14: (a) Sinusoidal tracking results of FO-AEF, PID and BO controllers. (b) Tracking errors of FO-AEF, PID and BO controllers. (c) Boxplot graphs of the tracking errors of FO-AEF, PID and BO controllers.

The mean and maximum errors for needle translation are 0.17 mm and 0.33 mm, for target positions of 0 and 10 mm. The mean and maximum errors for needle rotation are 1.30° and 3.65°, for target angles of 0 and 100°. The calculated mean linear-to-rotary motion ratio δ of 1 mm: 10.407° confirms the reliability of the proposed passive rotation mechanism. This rotation mechanism consistently achieves the desired ratio of 10°/mm and can be controlled using translational displacement data from the fiber-optic encoder.

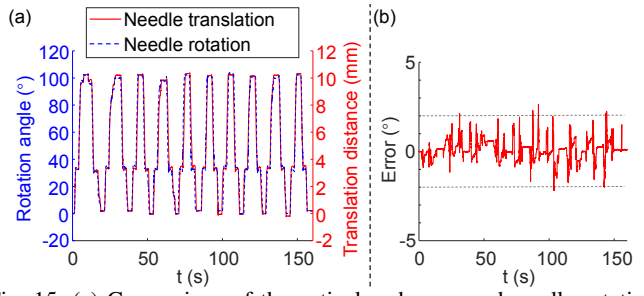

Fig. 15: (a) Comparison of theoretical and measured needle rotation angles: The red line shows needle displacement (0–10 mm) which can be multiplied by δ=10 for the theoretical needle rotation angle reference, while the blue line shows the measured needle rotation angle. (b) The error between the theoretical and measured needle rotation angles.

C. Evaluation of Needle Repeatability under an External Load

As shown in Fig. 16(a), the experimental setup was configured with the needle driver secured to the desktop using two bench clamps. For load application, the needle was linked to a 1 kg desk-mounted weight through a connector, producing an equivalent friction force of roughly 5 N. This friction force varies slightly during motion due to dynamic factors such as surface interactions. This setup effectively simulated axial resistance while also increasing the mechanical inertia of the needle system, thereby challenging control stability and response performance. Additionally, an EM sensor was attached to the opposite end of the needle, away from metallic objects, for real-time position measurement while minimizing interference from metals on the sensor's accuracy.

The needle driver was commanded to track a reference step signal (0 to 10 mm, repeated 10 times) under the FO-AEF controller. To achieve finer feedback resolution and better capture potential disturbances in this loaded scenario, an upgraded fiber-optic encoder with 0.25 mm resolution was employed for closed-loop control. The corresponding data was recorded by the EM sensor, as illustrated in Fig. 16(b). Results showed that positioning accuracy remains robust under this loaded condition, with a RMSE of 0.107 mm and a maximum error of 0.136 mm, representing a 37% improvement in accuracy compared to prior experiments conducted without the upgraded encoder. The FO-AEF controller's adaptive fuzzy logic mitigated variable friction and inertia-induced disturbances (e.g., oscillations), while the encoder's enhanced resolution reduced quantization errors, ensuring stable control without slippage or overshoot. No loss of grasp was observed, confirming the pre-clamped gripper's reliability under load.

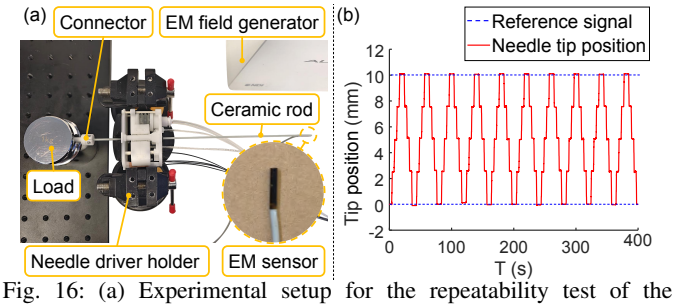

Fig. 16: (a) Experimental setup for the repeatability test of the needle driver under external load. (b) Measured tip displacement over repeated cycles.

D. Decoupling Effectiveness between Independent Translation and Translation with Passive Rotation

The total stroke of the slider on the needle driver is 6.6 mm. It is divided into two parts by a dividing line located at 4.15 mm. Motion type II spans 0-4.15 mm while the motion type I span 4.15-6.6 mm, as shown in Fig. 17(a). The decoupling effectiveness between the two motion types was evaluated by programming the needle driver to repeatedly perform motion type II for 10 times before switching to motion type I using the switching signal from the sensing system as feedback. An EM sensor was attached to the needle tip to record the real-time experimental results, as depicted in Fig. 17(b).

During implementation of motion type II (0-66s), the needle experienced translation between 0 mm and 4.15 mm and rotation between 0 and 41.5°. The root-mean-square steady-state error of the slider with respect to the target (i.e. dividing line) is 0.018 mm, indicating that the proposed sensing system can effectively limit the range of needle translation with passive rotation to 0-4.15 mm. During implementation of motion type I (66s-100s), the needle translation ranged between 4.15 mm and 6.6 mm while the needle rotation remained completely unchanged at 41.5°. The root-mean-square error between the slider's motion and the dividing line was 0.021

IEEE Transactions on Robotics (T-RO) paper, presented at ICRA 2026, Vienna, Austria. Cite as T-RO paper.

mm. These small RMS errors on both sides of the dividing line demonstrate that the dividing line can serve as a reliable absolute position reference, enabling accurate motion type switching and providing a consistent baseline for eliminating cumulative positioning errors during closed-loop control.

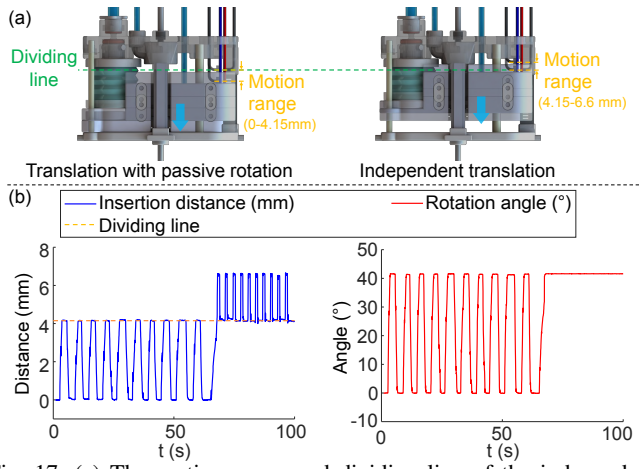

Fig. 17: (a) The motion range and dividing line of the independent translation and translation with passive rotation. (b) The experimental result of the decoupling effectiveness test, with the dividing line positioned at 4.15 mm.

E. Hysteresis Evaluation

We conducted an experiment to evaluate hysteresis between the master-side syringe and the follower-side needle driver, using the setup shown in Fig. 18(a). In each trial, the needle was commanded to move from 0 mm to 4 mm. We performed ten repeated tests using 2 m and 10 m transmission tubes, respectively. Master-side syringe displacement was measured from stepper motor pulses recorded by the STM32, and follower-side bellows-based actuator displacement was measured using the needle driver's integrated encoder.

For the 2 m tube, latency ranged from 0.10 to 0.36 s, with an average of 0.23 s. For the 10 m tube, latency ranged from 0.20 to 0.48 s, with an average of 0.31 s. The results indicate that although longer tubes increase the system's equivalent damping and thereby degrade raw performance, the performance difference observed between 2 m and 10 m tube lengths remains minimal. This can be attributed primarily to the incompressible nature of water. Furthermore, the proposed needle driver system incorporates an array of sensors to ensure that any hysteresis introduced by the hydraulic teleoperation does not compromise overall positioning accuracy.

F. Gripper Evaluation

The performance of the silicone diaphragm-based grippers were experimentally verified by the experimental setups shown in Fig. 19. During the first experiment, each of the static and moving grippers was fixed onto the bench clamp, and pressures of 0 kPa, 60 kPa, and -60 kPa were applied through a pipe. The changes of the silicone diaphragm in the static and moving grippers from the top view are shown in Fig. 19(a). It can be seen that the static gripper produces an irregular shrinkage under positive pressure and returns to its initial state

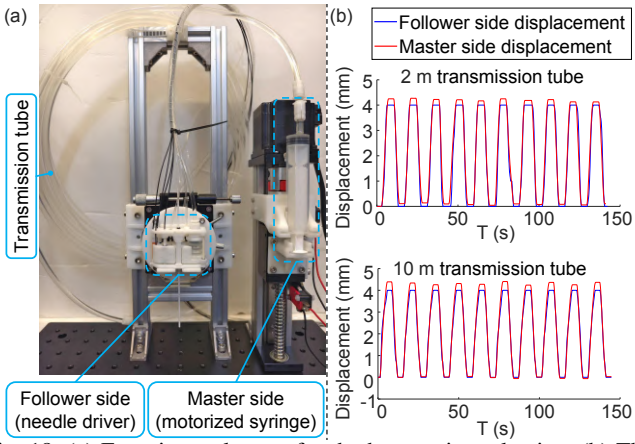

Fig. 18: (a) Experimental setup for the hysteresis evaluation. (b) The experimental result of the master and follower side displacement against time, with 2 m and 10 m transmission tube, respectively.

under negative pressure. The moving gripper with its added fillet feature was capable of radial shrinkage and expansion under positive and negative pressures, respectively, matching our FEA simulation results.

In addition, we evaluated the pressure–clamping force curves, pressure tolerance, and manufacturing success rates of grippers with different hardness levels silicone. As shown in Fig. 19(c), higher hardness yields greater pressure tolerance and clamping force. However, it also reduces flowability during molding, leading to bubble entrapment and consequently lower manufacturing success rates. In our tests, Shore 20A silicone balanced ease of fabrication (80-90% success) with adequate performance for our prototype, achieving the desired clamping force of 11 N without irregular shrinkage. Shore 30A silicone exhibited improved gripper mechanics over 20A, tolerating 300 kPa and delivering a maximum clamping force of 15 N, but with a slightly lower manufacturing success rate (70%). Shore 40A silicone provided good hardness for higher pressure tolerance (400 kPa) and clamping strength, with a reasonable success rate (50%), making it suitable for enhanced durability. Shore 50A silicone was very stiff, offering superior pressure resistance (500 kPa), but its poor flowability led to low success rates (12.5%) and frequent defects like bubbles or breakage during molding. Based on these results, we selected Shore 40A silicone as an optimal compromise, as it combines high manufacturability with improved pressure tolerance and clamping force.

Based on the Shore 40A silicone, the clamping force of the grippers was evaluated. A force sensor (ZP100, AIGU, Hong Kong) was attached to a motorized ball screw, while the grippers that hold a ceramic rod are connected to the bench clamp. For safety and durability reasons, the working principle of the gripper is set to 300kPa. With the force sensor probe and the ceramic rod aligned, the ceramic rod was pushed at a constant speed until it slipped off. This process was repeated 10 times and the results are depicted in Fig. 19(d). The static and moving gripper consistently offer a clamping force of at least 5.5 N and 16 N, respectively.

IEEE Transactions on Robotics (T-RO) paper, presented at ICRA 2026, Vienna, Austria. Cite as T-RO paper.

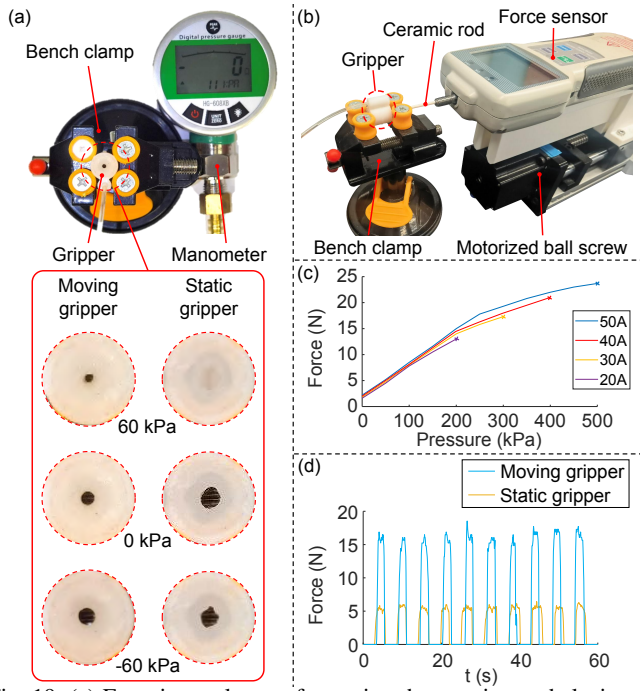

Fig. 19: (a) Experimental setup for testing the opening and closing of the grippers under different pressures and the corresponding results. (b) Experimental setup for evaluating the grippers' clamping force. (c) Pressure–clamping force curves for grippers fabricated from Shore 20A–50A silicone. (d) Force sensing data of the static and moving grippers in 10 repeated tests.

G. Actuator Force and Needle Insertion Force Evaluation

Although the proposed moving gripper has demonstrated a clamping force of approximately 11 N, it remains essential to verify whether the bellows-based actuator can generate sufficient force to successfully insert the needle. As depicted in Fig. 20(a), the force sensor and the needle driver were each fixed to separate bench clamps. The bottom cover of the needle driver was removed, allowing the bellows-driven slider to establish direct contact with the force sensor. The pressure applied to the bellows was gradually increased from 0 to 300 kPa, and the corresponding data recorded were shown in Fig. 20(a). The output force of the bellows-based actuator reaches up to 40 N at a pressure of 300 kPa, which significantly exceeds the clamping force of the moving gripper.

To explore the actual needle insertion force provided by the needle driver, an active needle insertion experiment was conducted with the gripper operating at 300 kPa. As depicted in Fig. 20(b), the needle driver was fixed on an aluminium profile frame through a 3D printed part, while the force sensor (ZNLBM, IIX, China) was attached to an optical breadboard. The force sensor was positioned beneath the needle driver, with the needle connected to the sensor via a connector, ensuring direct force transmission. After compensating for the needle's own weight, the needle driver was programmed to execute 10 repeated insertion actions, thus exerting force on the force sensor. In each insertion action, the needle driver provides insertion force ranging between 15 and 16 N, satisfying the performance criterion of at least 10 N insertion force.

To measure the maximum torque of the needle driver, the driver was mounted on a fixed frame, and a torque sensor (ZNNT, 1 N·m, China) was attached to a needle shaft with a 2 mm diameter. Controlled hydrostatic pressure was then applied to the bellows-based actuator to drive the slider, enabling the hybrid gear to apply torque to the needle. Measurements were repeated across 10 trials. As shown in Fig. 20(c), with the 2 mm diameter needle, the passive rotation mechanism produced a minimum torque of 15 N·mm and a maximum torque of 16 N·mm during steady motion. The measured torque indicates that the proposed gripping mechanism applies a tangential driving force of 16 N to the needle without stalling or causing significant slippage, and this force significantly exceeds typical soft tissue resistance.

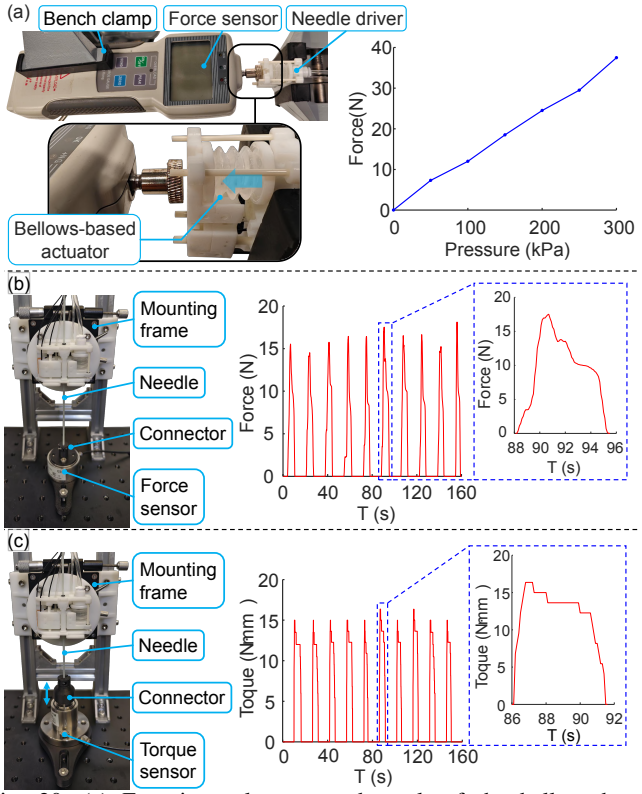

Fig. 20: (a) Experimental setup and result of the bellows-based actuator output force evaluation at different hydrostatic pressures. (b) Experimental setup and results for needle insertion force evaluation. (c) Experimental setup and results for needle rotation torque evaluation.

H. Phantom Study for Needle Translation with Passive Rotation

To better demonstrate the effect of passive rotation in reducing needle deflection and tissue resistance during a needle insertion process, the needle driver was commanded to execute motion type I and motion type II to insert the needle into a customized multi-layer phantom model. The phantom model consists of transparent simethicone with a viscosity of 1 million centistokes (cS) to simulate the muscle tissue, and a 1 mm thick silicone film with a Shore hardness rating of 20A to simulate the skin.

IEEE Transactions on Robotics (T-RO) paper, presented at ICRA 2026, Vienna, Austria. Cite as T-RO paper.

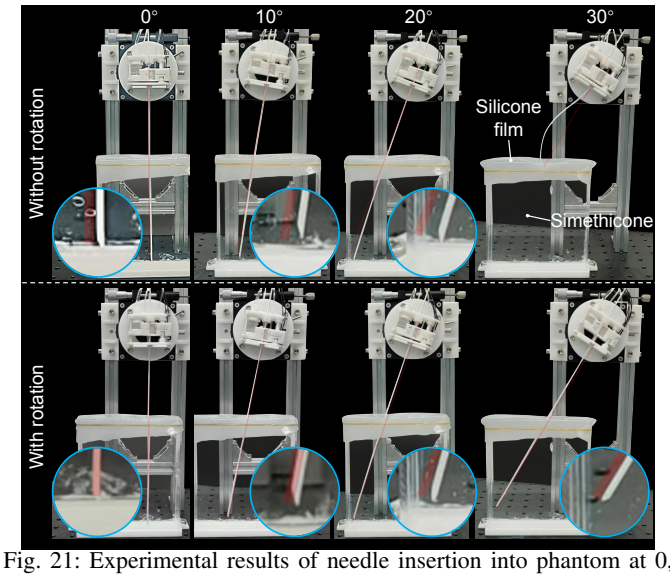

Fig. 21: Experimental results of needle insertion into phantom at 0, 10, 20, and 30 degrees under motion type I (independent translation without passive rotation) and motion type II (translation with passive rotation). The red line denotes the straight reference trajectory.

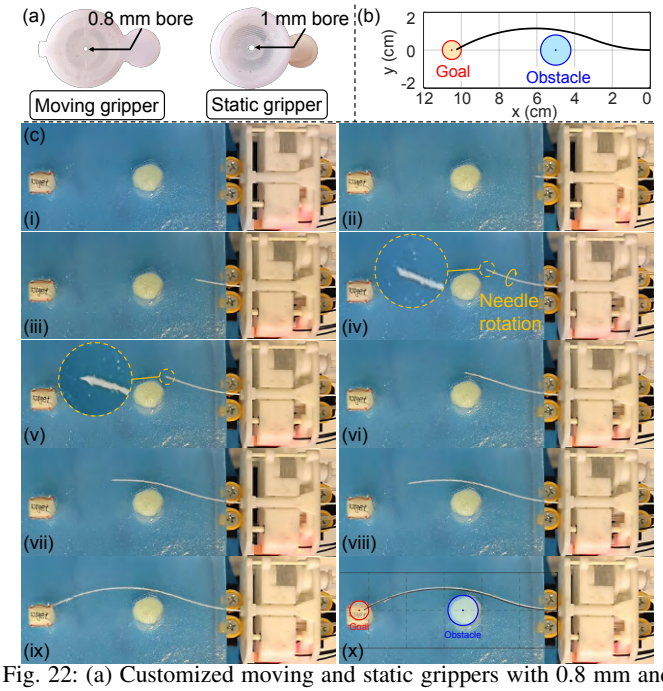

Fig. 22: (a) Customized moving and static grippers with 0.8 mm and 1 mm diameter bores, respectively, to accommodate flexible bevel-tipped needles. (b) Desired needle trajectory. (c): (i) Initial position; (ii)-(iv) The needle driver inserts the needle without rotation for 30 mm; (iv) Bevelled tip needle before rotation; (v) Bevelled tip needle after 180° rotation; (vi)-(ix) The needle driver inserts the needle without rotation for 70 mm; As the direction of the bevelled tip is rotated 180°, the needle steers in the opposite direction. (x) Comparison of actual and desired needle trajectories.

The needle insertion for each motion type was performed at four angles: 0°, 10°, 20°, and 30°. The angle was adjusted for the needle driver relative to the phantom model using a rotating base platform to which the needle drivers were mounted. The corresponding experimental needle tip positions are depicted in Fig. 21. The red line in the figure is the extension line from the centerline of the needle driver, indicating the reference straight needle trajectory in the phantom model, while the white line is the actual needle path.

Needle deflection is evaluated by determining the normal distance between the reference trajectory and the actual needle tip position according to the image data captured by the camera. The needle could be smoothly inserted at an inclination of 0°, 10°, and 20° with maximum deflection of 2.77 mm, 3.64 mm, and 5.45 mm from the desired trajectory when there was no needle rotation. However, when the angle of inclination reached 30°, the needle underwent a severe deformation in penetrating the silicone membrane, which in turn prevented further insertion. When the needle with passive rotation was inserted at 0°, 10°, 20°, and 30°, successful needle penetration in all angle cases and normal distance of 0.36 mm, 1.36 mm, 2.72 mm, and 2.63 mm, respectively. The results confirm that needle insertion with passive rotation was able to not only reduce the needle deflection, but also reduces tissue resistance especially during the skin penetration stage.

I. Phantom Study for Flexible Needle Steering

To demonstrate that combining independent translation (motion type I) and rotation (motion type III) enables a flexible needle to follow a nonlinear trajectory in tissue, an in-vitro experiment was conducted using a 0.8 mm ABS tube with a 45° beveled tip as the flexible needle, inserted into a 6% agar phantom. A moving gripper with 0.8 mm inner diameter and a static gripper with 1 mm inner diameter were fabricated to accommodate the size of the flexible needle, as shown in Fig. 22(a). The desired trajectory, generated in MATLAB using Webster et al.'s modeling approach [42], is depicted in Fig. 22(b). The needle navigates this path to avoid obstacles and reach a target by adjusting insertion depth and bevel tip orientation. A spherical obstacle (8 mm radius sponge cylinder) was embedded in the phantom to simulate obstacle avoidance. The needle driver, fixed by a vise, was controlled by a pre-programmed STM32 MCU script executing the MATLAB-generated trajectory through a sequence of translation and rotation steps. The sequence of actions applied to the needle consists of the following steps:

(1) The flexible needle is inserted for 30 mm using motion type I. As depicted in Fig. 22(b)(i)-(iv), the needle steers downward as it advances, due to the interaction between the upward-beveled tip and the surrounding tissue.

(2) The flexible needle is then rotated by 180° using motion type III. As shown in Fig. 22(b)(v)-(vi), this rotation reorients the beveled tip to face downward, with net-zero displacement in its translation.

(3) The flexible needle is finally inserted for 70 mm using motion type I. As illustrated in Fig. 22(b)(vii)-(ix), the needle now steers upward as it advances, completing the desired trajectory through the tissue.

As shown in Fig. 23, the experiments were repeated 10 times to establish statistical significance, with the needle starting from the same entry point each time. Results showed successful obstacle avoidance in all trials, with the needle reaching the target goal. Trajectory consistency is evaluated

IEEE Transactions on Robotics (T-RO) paper, presented at ICRA 2026, Vienna, Austria. Cite as T-RO paper.

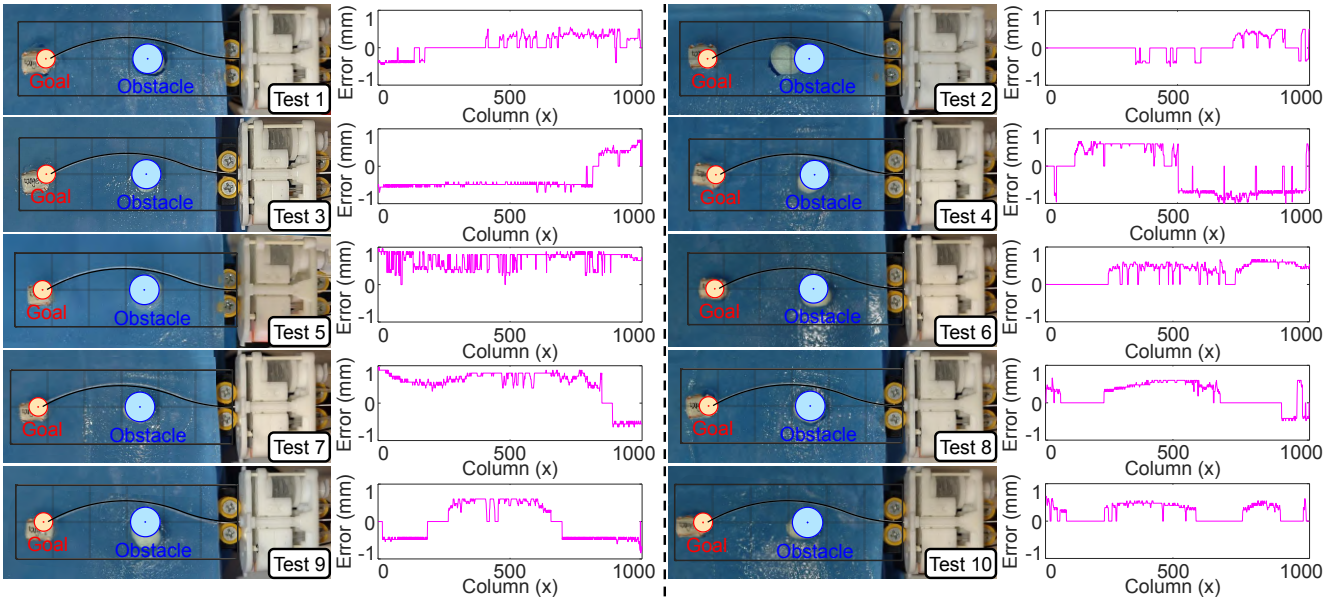

Fig. 23: Trajectories of the flexible needle across 10 independent tests, with the deviation between the actual and target trajectories at each pixel column displayed to the right of each test's trajectory plot.

by computing the vertical pixel-wise difference between the actual needle trajectory and the reference trajectory according to the image data captured by the camera. Despite factors such as variations in phantom texture and needle driver operation errors, which resulted in a maximum error of 0.98 mm, the average error of just 0.35 mm reflects a high degree of consistency between the needle trajectory and the reference trajectory.

To replicate clinical scenarios, we created a 6% agar liver phantom with an irregularly shaped sponge block as a simulated tumor, positioned behind vascular structures (hepatic artery and portal vein) to mimic obstacle avoidance. Despite the challenges flexible needles face in penetrating denser tissues, such as fat and muscle layers, to reach the liver, our concentric needle system demonstrates practical feasibility in clinical settings. As shown in Fig. 24, the concentric needle driver comprises two cascaded drivers: the lower one actuates the rigid needle, and the upper one drives the flexible needle. Since the needle driver's ability to actuate the rigid needle has been validated in prior sections, we focus on the flexible needle's navigation in the liver. Assuming the rigid needle has penetrated the fat and muscle layers, it is positioned directly above the liver tissue in the experimental setup. The spacing between the two drivers determines the insertion depth of the rigid needle, which incidentally highlights the advantage of our needle driver's compact size (only 3.8 cm in height), enabling compact integration and minimal overall system footprint for such multi-stage configurations. In this experiment, the flexible needle successfully steered around the vascular obstacles to reach the expected target position (verified via post-insertion imaging).

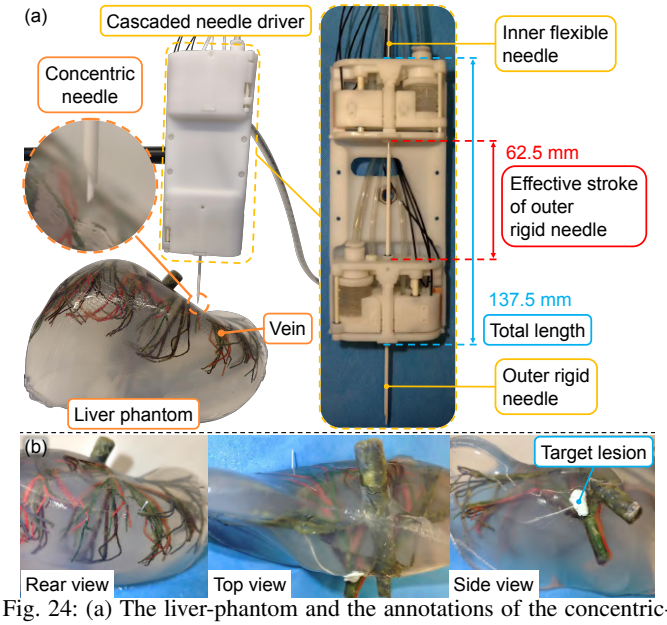

Fig. 24: (a) The liver-phantom and the annotations of the concentric-needle driver system. (b) Rear, top, and side views of the experiment, showing the internal flexible needle steering around the vascular network to reach the target.

J. MR-Compatibility Test

A series of tests were performed in the MR room to confirm the MRI compatibility of the robotic needle driver. The needle driver and a standard MRI water phantom were placed on the patient bed of the MR scanner while the master controller was placed in the control room. Static MR scans were performed using the T1-weighted fast field echo (FFE) sequences for the following cases, namely 1) phantom only (baseline), 2) phantom and stationary robotic needle driver, and 3) phantom and robotic needle driver actuating a ceramic needle, respectively.

Fig. 25(b) shows images in the axial plane along the surface of the agar phantom for the two cases with and without the robot. The presence and continuous actuation of the robot do not cause any significant or visible artifact/distortion relative to the baseline. The corresponding signal-to-noise ratio (SNR) for

IEEE Transactions on Robotics (T-RO) paper, presented at ICRA 2026, Vienna, Austria. Cite as T-RO paper.

TABLE II: Comparisons between the proposed design and existing MRI-compatible needle drivers

Author	MR-compatibility	Motion type	Size (L×W×H)	Stroke	Insertion force	Actuator force	Accuracy
Hungr et.al. [17]	MR-conditional	Translation only	14 cm H	3.5 cm	-	-	0.5 mm
Navarro et.al. [15]	MR-conditional	Translation only	26 cm H	7.5 cm	$>$ 3N	-	$<$ 1 mm
Comber et.al. [21]	MR-safe main body, MR-conditional encoder	Translation only	4.5 × 4.5 × 9.5 cm	Infinite	-	45 N	0.025 mm
Pfeil et.al. [22]	MR-safe	Translation only	2.92 × 2.92 × 4 cm	Infinite	2N	-	-
Frishman et.al. [44]	MR-safe	Translation only	12 cm H	Infinite	25 N	-	-
Groenhuis et.al. [45]	MR-safe	Translation only	10.7 cm H	11.1 cm	60 N	-	0.1 mm
Qiu et.al. [23]	MR-safe	Translation only	4.5 × 4.5 × 11 cm	Infinite	6 N	>50 N	0.5 mm
Li et.al. [46]	MR-conditional	Translation and rotation	11 × 13 × 29.2 cm	13 cm	20 N	-	$<$ 1 mm
Wu et.al. [18]	MR-conditional	Translation and rotation	18.6 cm H	15 cm	-	-	0.8 mm and 2.25°
Comber et.al. [29]	MR-safe main body, MR-conditional encoder	Translation and rotation	8.9 × 8.9 × 33 cm	Infinite	-	45 N	0.025 mm and 0.018°
Proposed design	MR-safe	Translation and rotation	2.2 × 5.3 × 3.8 cm	Infinite	>10 N	>40 N	0.17 mm and 1.3°

Note: 'L', 'W', and 'H' refer to length, width, and height of the needle driver. Height denotes the dimension along the needle axis.

each case was also calculated [43], as shown in Fig. 25(b). The SNR drops due to the robot presence and robot actuation are less than 0.1%, quantitatively confirming the MR compatibility and safety of the robot.

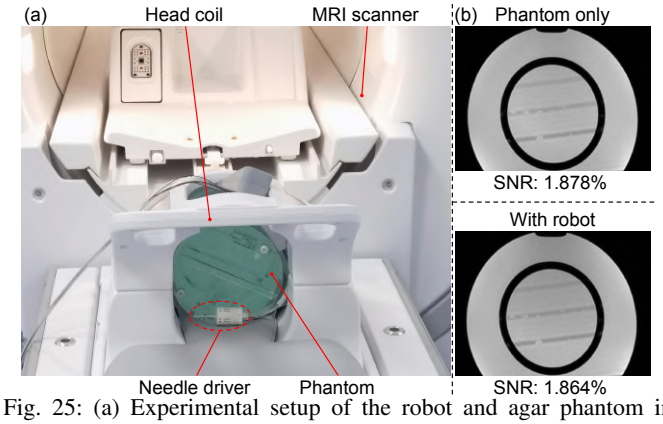

Fig. 25: (a) Experimental setup of the robot and agar phantom in a 1.5T MRI; (b) MR images of a phantom in two cases, with and without the robot.

V. Discussion

Existing MR-safe needle drivers can be categorized by their motion patterns, namely continuous and inchworm-type. The former typically features a limited stroke while the latter enables infinite stroke. The proposed needle driver utilizes the inchworm-type motion for its needle translation, allowing it to accommodate needles of varying lengths through repeated grip-move-release cycles. Unlike most pneumatic stepper actuators [45], which convert pulses of constant-pressure air into precise stepped linear motion, our soft bellows-based actuator gradually expands with increased pressure, allowing for smooth and impact-free needle insertion. This is particularly advantageous for long-distance insertions in percutaneous procedures, such as flexible needle intervention and concentric tube actuation, where existing continuous drivers are limited by fixed strokes and bulky sizes [15], [17], [44]. Fixed-stroke drivers also face several limitations, including limited adaptability to varying needle lengths, the inability to incorporate "pause-release" mechanisms that could help mitigate tissue damage (in organs such as the liver and lungs) caused by respiratory motion during insertion, and challenges in integration within confined MRI bores due to their elongated designs and higher mechanical complexity. To manage potential cumulative positioning errors that could accumulate over multiple cycles, the fiber optics-based sensing system incorporates a switching signal as an absolute position reference at the dividing line (Section II-D). This signal not only facilitates switching between motion types (e.g., independent translation and translation with passive rotation) but also enables cumulative error correction for each cycle, ensuring long-term accuracy during extended operations.

Compactness is also a critical factor, as needle drivers must be operated within the confined space of the MRI bore or MR imaging coil. The continuous needle drivers require a height longer than the needle itself [15], [17], [46], leading to increased volume, which is less conducive to system integration. Compared to continuous needle drivers, inchworm-type designs are significantly smaller and more compact, making them better suited for such restricted environments. Current state-of-the-art MR-safe needle drivers with the inchworm design, such as those by Comber et al. [21] and Pfeil et al. [22], feature compact size with heights of 9.5 cm and 4 cm, respec-

tively. However, they lack the rotational DOF, which provide significant advantages such as reducing needle deflection, enabling non-linear trajectories, and enhancing tissue penetration efficiency. Most existing MRI-safe needle actuators lack this degree of freedom. Incorporating the rotational DOF often comes at the expense of increased size, making them challenging to be deployed in confined environments such as MRI bores or head coils. For example, the design by Comber et al. [29] achieves only sequential insertion and rotation functions, and its 33 cm height limits further applications within MRI scanners, especially those that demand skull-mounted or body-mounted setups. The 2 DOFs needle driver proposed by Wu et al. [18] is comparatively more compact, but it still measures 20 cm in height, has a limited stroke, relies on the MR-conditional piezoelectric motors and features bulky transmission mechanisms. To address this trade-off, our proposed MR-safe needle driver achieves both sequential and simultaneous translational and rotational motions while maintaining an exceptionally compact design, measuring only 3.8 cm in height. This compactness facilitates easy integration into various needle positioning platforms and ensures flexible operation in restricted spaces.

Achieving compactness is essential for integration into space-constrained MR environments without compromising the system's ability to deliver sufficient insertion force. While inchworm-type needle drivers offer broader applicability and compact designs, slippage between the needle and gripper often limits their insertion force. For instance, the 4 cm needle driver by Pfeil et al. [22] and the 11 cm needle driver by Qiu et al. [23] achieve insertion forces of only 2 N and 6 N, respectively. In contrast, our proposed 3.8 cm needle driver, the most compact in the needle axis direction, delivers over 16 N, suitable for most soft tissue interventions [36].

Existing designs using flat film grippers [21], [23], [29], [47] provide limited contact surface, reducing the efficiency of converting applied pressure into clamping force. Unlike these, Frishman et al. [44] used a collet-based gripper with a single-acting piston, achieving up to 25 N clamping force but resulting in a bulkier design with potential retraction force issues under high loads, risking gripper jamming. Our pre-clamped silicone diaphragm-based gripper, fully fitted to the needle, enhances clamping force efficiency while ensuring reliable gripping and releasing. In clinical scenarios involving bodily fluids (e.g., blood), which may reduce friction and grasping force during needle withdrawal (typically requiring only 0.5-1 N [48], [49]). Preliminary tests show that the gripper's effective force attenuates to 40-50% of its dry-state value (6-8 N in 300 kPa), still sufficient for single-insertion tasks. For multi-insertion procedures, future work will explore materials with higher friction coefficients, to enhance clamping under hydraulic pressure and reduce sensitivity to friction loss; integrated drying mechanisms (e.g., absorbent elements at the bottom cover of the needle driver); and specialized surface textures or coatings (e.g., micro-patterns or hydrophobic/anti-slip treatments) on the diaphragms to maintain grip in wet conditions, enabling greater insertion force overall.

In addition to sufficient insertion force, precise needle position control is also significant for successful percutaneous procedures. The positioning accuracy of existing state-of-the-art needle drivers in Table II typically ranges from 0.1 to 1 mm. Comber et al. demonstrate remarkable accuracy, achieving 0.025 mm and 0.018° in the translational and rotational DOFs, respectively [29]. This exceptional performance is attributed to their use of MR-conditional optical encoders with resolutions as high as 0.05 mm and 0.072°. Nevertheless, although not explicitly validated in their study, the encoders involve electronic components which are likely to affect the quality of MR images. The MR-safe encoder's resolution is limited by fiber optic constraints, as MR-safe designs require long-distance light signal transmission, with the smallest viable fiber core diameter being 0.25 mm. Initially, laser-cutting limitations and signal attenuation restricted resolution to 0.5 mm. To address this, we switched to red wax 3D printing for a 0.25 mm grating scale and upgraded the laser source from 1.5 W to 3 W, achieving a resolution of 0.25 mm with reliable signal detection. Repeatability tests under load showed a reduced RMSE of 0.107 mm, a 37% improvement from 0.17 mm. Future work could explore custom finer fibers and 0.1 mm gratings to approach 0.1 mm resolution, though signal loss must be carefully managed.

Our needle driver employs a low-cost MR-safe fiber optic-based encoder and introduced the FO-AEF controller to achieve an average needle translation error of 0.17 mm and an average rotation error of 1.3°, which is comparable to the current best MR-safe systems and sufficient to meet the requirements of most clinical applications. The system's precision makes it highly suitable for a range of diagnostic and therapeutic procedures requiring millimeter translational accuracy and minimal rotational deviation. For example, liver or lung biopsies, prostate brachytherapy, abdominal interventions, neurosurgery (e.g., tumor ablation), and spinal injections. However, certain high-precision or safety-critical procedures demand stricter tolerances, where current error margins could pose risks without additional safeguards, such as intraoperative imaging or hybrid manual-robotic control. Examples include vascular interventions, microsurgical procedures, and pediatric applications.

Although the complete needle driver has not been verified as biocompatible, the material of the parts used in contact with the needle has been verified to be biocompatible, including the needle guide based on PEEK material and the silicone diaphragm for the grippers. However, the photosensitive resin components are limited to disinfectant immersion. To enable full steam sterilization and clinical readiness, we plan to switch to medical-grade PEEK for structural parts while retaining silicone for flexible elements like bellows and grippers, ensuring biocompatibility (e.g., ISO 10993 compliance). This transition, estimated at 6-12 months, involves redesign for injection molding (2-3 months), testing for mechanical performance and sealing (3-6 months), and certification preparations (1-2 months). Challenges include maintaining watertight PEEK-silicone seals under high temperatures and ensuring bellows flexibility. While PEEK increases prototyping costs (5-10 times higher than resin), injection molding will reduce per-unit costs, preserving flexibility and sealing efficacy.

VI. Conclusion

It is challenging for existing needle drivers to properly balance MR compatibility, compactness, versatility in output motion types, and insertion force. As a result, most needle drivers remain unsuitable for clinical adoption in MRI-guided needle interventions, and many MRI-compatible robotic systems remain as positioning platforms that require manual needle insertion. This work introduces the design and control of a novel MR-safe single bellows-based hydraulic needle driver, constructed from low-cost additive manufacturing materials. As the world's shortest needle driver, it simultaneously achieves smooth motion and high output force under a closed-loop AEF-based control framework, showing great potential for direct integration with most existing needle positioning platforms which can help advance MR-safe robotic systems into a new stage of intraoperative MRI-guided needle interventions with potentially more automated capabilities. The highly compact and reliable motion decoupling and switching mechanisms enable the needle driver to achieve three different motion types, including independent needle translation, translation with passive rotation, and independent needle rotation, leading to various capabilities such as needle insertion with reduced deflection and reduced tissue resistance as well as flexible bevel-tipped needle steering. In our future work, the needle driver will be further optimized with enhanced sensing resolution, better sterilizability, and additional diagnostic and therapeutic capabilities to improve its potential for clinical adoption. We will also refine the design of MR-safe quick-connect water tube fittings, ideally making them unidirectional to enhance system reliability. We will also integrate the needle driver with a needle positioning platform to realize intraoperative and potentially automated MRI-guided needle navigation.

References

[1] K. Cleary and T. M. Peters, "Image-guided interventions: technology review and clinical applications," *Annual review of biomedical engineering*, vol. 12, no. 1, pp. 119–142, 2010.

[2] J. Barkhausen, T. Kahn, G. A. Krombach, C. K. Kuhl, J. Lotz, D. Maintz, J. Ricke, S. O. Schönberg, T. J. Vogl, F. K. Wacker *et al.*, "White paper: interventional mri: current status and potential for development considering economic perspectives, part 1: general application," in *RöFo-Fortschritte auf dem Gebiet der Röntgenstrahlen und der bildgebenden Verfahren*, vol. 189, no. 07. © Georg Thieme Verlag KG, 2017, pp. 611–623.

[3] W. Meinhold, D. E. Martinez, J. Oshinski, A.-P. Hu, and J. Ueda, "A direct drive parallel plane piezoelectric needle positioning robot for mri guided intraspinal injection," *IEEE Transactions on Biomedical Engineering*, vol. 68, no. 3, pp. 807–814, 2020.

[4] G. Li, H. Su, G. A. Cole, W. Shang, K. Harrington, A. Camilo, J. G. Pilitsis, and G. S. Fischer, "Robotic system for mri-guided stereotactic neurosurgery," *IEEE transactions on biomedical engineering*, vol. 62, no. 4, pp. 1077–1088, 2014.

[5] E. Franco, D. Brujic, M. Rea, W. M. Gedroyc, and M. Ristic, "Needle-guiding robot for laser ablation of liver tumors under mri guidance," *IEEE/ASME Transactions on Mechatronics*, vol. 21, no. 2, pp. 931–944, 2015.

[6] D. Stoianovici, C. Jun, S. Lim, P. Li, D. Petrisor, S. Fricke, K. Sharma, and K. Cleary, "Multi-imager compatible, MR safe, remote center of motion needle-guide robot," *IEEE Transactions on Biomedical Engineering*, vol. 65, no. 1, pp. 165–177, 2017.

[7] Z. Guo, Z. Dong, K.-H. Lee, C. L. Cheung, H.-C. Fu, J. D. Ho, H. He, W.-S. Poon, D. T.-M. Chan, and K.-W. Kwok, "Compact design of a hydraulic driving robot for intraoperative mri-guided bilateral stereotactic neurosurgery," *IEEE Robotics and Automation Letters*, vol. 3, no. 3, pp. 2515–2522, 2018.

[8] Z. He, Z. Dong, G. Fang, J. D.-L. Ho, C.-L. Cheung, H.-C. Chang, C. C.-N. Chong, J. Y.-K. Chan, D. T. M. Chan, and K.-W. Kwok, "Design of a percutaneous MRI-guided needle robot with soft fluid-driven actuator," *IEEE Robotics and Automation Letters*, vol. 5, no. 2, pp. 2100–2107, 2020.

[9] L. Chen, T. Paetz, V. Dicken, S. Krass, J. A. Issawi, D. Ojdanić, S. Krass, G. Tigelaar, J. Sabisch, A. v. Poelgeest *et al.*, "Design of a dedicated five degree-of-freedom magnetic resonance imaging compatible robot for image guided prostate biopsy," *Journal of Medical Devices*, vol. 9, no. 1, p. 015002, 2015.

[10] D. Stoianovici, C. Kim, D. Petrisor, C. Jun, S. Lim, M. W. Ball, A. Ross, K. J. Macura, and M. E. Allaf, "Mr safe robot, fda clearance, safety and feasibility of prostate biopsy clinical trial," *IEEE/ASME Transactions on Mechatronics*, vol. 22, no. 1, pp. 115–126, 2016.

[11] V. Groenhuis, F. J. Siepel, J. Veltman, J. K. van Zandwijk, and S. Stramigioli, "Stormram 4: An mr safe robotic system for breast biopsy," *Annals of biomedical engineering*, vol. 46, pp. 1686–1696, 2018.

[12] H. Ranjan, M. Van Hilten, V. Groenhuis, J. Verde, A. Garcia, S. Perretta, J. Veltman, F. J. Siepel, and S. Stramigioli, "Sunram 7: An mr safe robotic system for breast biopsy," in *2023 IEEE/RSJ International Conference on Intelligent Robots and Systems (IROS)*. IEEE, 2023, pp. 10 281–10 288.

[13] J. Simonelli, Y.-H. Lee, C.-W. Chen, X. Li, S. Mikaiel, D. Lu, H. H. Wu, and T.-C. Tsao, "Hydrostatic actuation for remote operations in mr environment," *IEEE/ASME Transactions on Mechatronics*, vol. 25, no. 2, pp. 894–905, 2019.

[14] E. Franco, M. Rea, W. Gedroyc, and M. Ristic, "Control of a master–slave pneumatic system for teleoperated needle insertion in mri," *IEEE/ASME Transactions on Mechatronics*, vol. 21, no. 5, pp. 2595–2600, 2016.

[15] D. Navarro-Alarcon, S. Singh, T. Zhang, H. L. Chung, K. W. Ng, M. K. Chow, and Y. Liu, "Developing a compact robotic needle driver for mri-guided breast biopsy in tight environments," *IEEE Robotics and Automation Letters*, vol. 2, no. 3, pp. 1648–1655, 2017.

[16] Z. Fang, C. Xu, H. Gao, D. T.-M. Chan, W. Yuan, and H. Ren, "Head-mounted hydraulic needle driver for targeted interventions in neurosurgery," in *2024 IEEE/RSJ International Conference on Intelligent Robots and Systems (IROS)*. IEEE, 2024, pp. 2429–2435.

[17] N. Hungr, I. Bricault, P. Cinquin, and C. Fouard, "Design and validation of a CT-and MRI-guided robot for percutaneous needle procedures," *IEEE transactions on robotics*, vol. 32, no. 4, pp. 973–987, 2016.

[18] D. Wu, G. Li, N. Patel, J. Yan, G. H. Kim, R. Monfaredi, K. Cleary, and I. Iordachita, "Remotely actuated needle driving device for MRI-guided percutaneous interventions: Force and accuracy evaluation," in *2019 41st Annual International Conference of the IEEE Engineering in Medicine and Biology Society (EMBC)*. IEEE, 2019, pp. 1985–1989.

[19] Y. Wang, G. Liu, G. Li, K. Cleary, and I. Iordachita, "An mr-conditional needle driver for robot-assisted spinal injections: Design modifications and evaluations," in *2022 44th Annual International Conference of the IEEE Engineering in Medicine & Biology Society (EMBC)*. IEEE, 2022, pp. 3307–3312.

[20] G. Li, N. A. Patel, Y. Wang, C. Dumoulin, W. Loew, O. Loparo, K. Schneider, K. Sharma, K. Cleary, J. Fritz *et al.*, "Fully actuated body-mounted robotic system for mri-guided lower back pain injections: Initial phantom and cadaver studies," *IEEE robotics and automation letters*, vol. 5, no. 4, pp. 5245–5251, 2020.

[21] D. B. Comber, J. E. Slightam, E. J. Barth, V. R. Gervasi, and R. J. Webster III, "Design and precision control of an mr-compatible flexible fluidic actuator," in *Fluid Power Systems Technology*, vol. 56086. American Society of Mechanical Engineers, 2013, p. V001T01A048.

[22] A. Pfeil, L. Barbe, B. Wach, A. Bruyas, F. Geiskopf, M. Nierenberger, and P. Renaud, "A 3d-printed needle driver based on auxetic structure and inchworm kinematics," in *International Design Engineering Technical Conferences and Computers and Information in Engineering Conference*, vol. 51807. American Society of Mechanical Engineers, 2018, p. V05AT07A057.

[23] Y. Qiu, H. Fang, J. Chen, J. Yan, Q. Ding, S. C. H. Yu, and S. S. Cheng, "An mr-safe robotic manipulator with hydraulic bellows actuators for spine procedures," *IEEE/ASME Transactions on Mechatronics*, 2023.

[24] H. Li, Y. Wang, Y. Li, and J. Zhang, "A novel manipulator with needle insertion forces feedback for robot-assisted lumbar puncture,"

The International Journal of Medical Robotics and Computer Assisted Surgery, vol. 17, no. 2, Art. no. e2226, 2021.

[25] N. Abolhassani, R. V. Patel, and F. Ayazi, "Minimization of needle deflection in robot-assisted percutaneous therapy," *The international journal of medical Robotics and computer assisted surgery*, vol. 3, no. 2, pp. 140–148, 2007.

[26] D. S. Minhas, J. A. Engh, M. M. Fenske, and C. N. Riviere, "Modeling of needle steering via duty-cycled spinning," in *2007 29th Annual International Conference of the IEEE Engineering in Medicine and Biology Society*. IEEE, 2007, pp. 2756–2759.

[27] Y.-J. Kim, S. B. Park, C.-H. Yoon, Y. Kim, H.-S. Kang, and Y.-H. Jo, "Robust deflected path planning method for superelastic nitinol coaxial biopsy needle: application to an automated magnetic resonance image-guided breast biopsy robot," *IEEE Transactions on Robotics*, vol. 38, no. 4, pp. 2220–2237, 2022.

[28] S. Patil, J. Burgner, R. J. Webster, and R. Alterovitz, "Needle steering in 3-d via rapid replanning," *IEEE Transactions on Robotics*, vol. 30, no. 4, pp. 853–864, 2014.

[29] D. B. Comber, J. E. Slightam, V. R. Gervasi, J. S. Neimat, and E. J. Barth, "Design, additive manufacture, and control of a pneumatic mr-compatible needle driver," *IEEE Transactions on Robotics*, vol. 32, no. 1, pp. 138–149, 2016.

[30] M. Harwood, S. J. Fahrenholtz, C. V. Wellnitz, A. Kawashima, and A. Panda, "Mri in adult patients with active and inactive implanted mr-conditional, mr-nonconditional, and other devices," *RadioGraphics*, vol. 44, no. 3, p. e230102, 2024.

[31] G. J. Vrooijink, M. Abayazid, S. Patil, R. Alterovitz, and S. Misra, "Needle path planning and steering in a three-dimensional non-static environment using two-dimensional ultrasound images," *The International journal of robotics research*, vol. 33, no. 10, pp. 1361–1374, 2014.

[32] D. B. Comber, E. J. Barth, and R. J. Webster III, "Design and control of an magnetic resonance compatible precision pneumatic active cannula robot," *Journal of Medical Devices*, vol. 8, no. 1, p. 011003, 2014.

[33] G. S. Gazelle, S. N. Goldberg, L. Solbiati, and T. Livraghi, "Tumor ablation with radio-frequency energy," *Radiology*, vol. 217, no. 3, pp. 633–646, 2000.

[34] A. M. Lozano and N. Lipsman, "Probing and regulating dysfunctional circuits using deep brain stimulation," *Neuron*, vol. 77, no. 3, pp. 406–424, 2013.

[35] G. Li, N. A. Patel, W. Liu, D. Wu, K. Sharma, K. Cleary, J. Fritz, and I. Iordachita, "A fully actuated body-mounted robotic assistant for mri-guided low back pain injection," in *2020 IEEE International Conference on Robotics and Automation (ICRA)*. IEEE, 2020, pp. 5495–5501.

[36] D. J. van Gerwen, J. Dankelman, and J. J. van den Dobbelsteen, "Needle–tissue interaction forces–a survey of experimental data," *Medical engineering & physics*, vol. 34, no. 6, pp. 665–680, 2012.

[37] A. F2503-13, *Standard Practice for Marking Medical Devices and Other Items for Safety in the Magnetic Resonance Environment*. West Conshohocken, PA, ASTM, 2013.

[38] Z. Huang, A. L. Gunderman, S. E. Wilcox, S. Sengupta, J. Shah, A. Lu, D. Woodrum, and Y. Chen, "Body-mounted mr-conditional robot for minimally invasive liver intervention," *Annals of Biomedical Engineering*, pp. 1–11, 2024.

[39] R. Tsumura, Y. Takishita, Y. Fukushima, and H. Iwata, "Histological evaluation of tissue damage caused by rotational needle insertion," in *2016 38th annual international conference of the IEEE engineering in medicine and biology society (EMBC)*. IEEE, 2016, pp. 5120–5123.

[40] H. Xiao, Q.-X. Meng, X.-Z. Lai, Z. Yan, S.-Y. Zhao, and M. Wu, "Design and trajectory tracking control of a novel pneumatic bellows actuator," *Nonlinear Dynamics*, vol. 111, no. 4, pp. 3173–3190, 2023.

[41] J. Chen, L. Deng, Z. Hua, W. Ying, and J. Zhao, "Bayesian optimization-based efficient impedance controller tuning for robotic interaction with force feedback," *IEEE Transactions on Instrumentation and Measurement*, vol. 72, pp. 1–10, 2023.

[42] R. J. Webster III, J. S. Kim, N. J. Cowan, G. S. Chirikjian, and A. M. Okamura, "Nonholonomic modeling of needle steering," *The International Journal of Robotics Research*, vol. 25, no. 5-6, pp. 509–525, 2006.

[43] N. E. M. Association *et al.*, "Determination of signal-to-noise ratio (snr) in diagnostic magnetic resonance imaging," *NEMA Standards Publication MS 1-2001*, 2001.

[44] S. Frishman, A. Kight, I. Pirozzi, M. C. Coffey, B. L. Daniel, and M. R. Cutkosky, "Enabling in-bore mri-guided biopsies with force feedback," *IEEE transactions on haptics*, vol. 13, no. 1, pp. 159–166, 2020.

[45] V. Groenhuis, F. J. Siepel, and S. Stramigioli, "Sunram 5: A magnetic resonance-safe robotic system for breast biopsy, driven by pneumatic stepper motors," in *Handbook of Robotic and Image-Guided Surgery*. Elsevier, 2020, pp. 375–396.

[46] M. Li, B. Gonenc, K. Kim, W. Shang, and I. Iordachita, "Development of an mri-compatible needle driver for in-bore prostate biopsy," in *2015 International Conference on Advanced Robotics (ICAR)*. IEEE, 2015, pp. 130–136.

[47] M. J. Musa, K. Sharma, K. Cleary, and Y. Chen, "Respiratory compensated robot for liver cancer treatment: Design, fabrication, and benchtop characterization," *IEEE/ASME Transactions on Mechatronics*, vol. 27, no. 1, pp. 268–279, 2021.

[48] A. Okamura, C. Simone, and M. O'Leary, "Force modeling for needle insertion into soft tissue," *IEEE Transactions on Biomedical Engineering*, vol. 51, no. 10, pp. 1707–1716, 2004.

[49] M. Mahvash and P. E. Dupont, "Mechanics of dynamic needle insertion into a biological material," *IEEE Transactions on Biomedical Engineering*, vol. 57, no. 4, pp. 934–943, 2010.

Yufu Qiu received his B.Eng. degree in automation from Guangdong University of Technology, Guangzhou, China, in 2021. He is pursuing the Ph.D. degree in the Department of Mechanical and Automation Engineering at The Chinese University of Hong Kong, Hong Kong, China. His research interests include the design and control of surgical robotic systems.

Haiyang Fang received his B.Eng. degree in automation from Anhui University, Hefei, China, in 2018. He is pursuing the Ph.D. degree in the Department of Mechanical and Automation Engineering at The Chinese University of Hong Kong, Shatin, Hong Kong, China.

Kwan Kit Lin is currently pursuing the Ph.D. degree in mechanical and automation engineering in The Chinese University of Hong Kong (CUHK). He also received the B.Eng. and M.Phil. degrees from the Department of Mechanical and Automation Engineering, CUHK. His current research interests include surgical robotics, soft robotics, and MR-compatible devices.

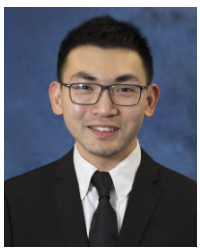

Shing Shin Cheng received the B.S. degree in mechanical engineering from the Johns Hopkins University, USA, in 2013, and the Ph.D. degree in robotics from the Georgia Institute of Technology, USA in 2018. He is currently an Associate Professor in the Department of Mechanical and Automation Engineering, The Chinese University of Hong Kong, Hong Kong. His research interests include flexible surgical robotics and image-guided surgical systems.